

**ADVANCED TURBULENCE MODELLING AND SIMULATION
IN VARIOUS FLUID FLOW HEAT TRANSFER AND
SURFACE CHEMISTRY PHENOMENA**

A DISSERTATION

*Submitted in partial fulfillment of the
requirements for the award of the degree*

of

MASTER OF TECHNOLOGY

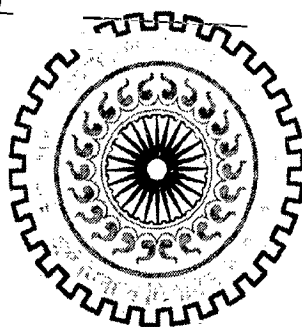
in

CHEMICAL ENGINEERING

(Industrial Pollution Abatement)

By

MAHARSHI SUBHASH



**DEPARTMENT OF CHEMICAL ENGINEERING
INDIAN INSTITUTE OF TECHNOLOGY ROORKEE
ROORKEE-247 667 (INDIA)**

JUNE 2007

CANDIDATE'S DECLARATION

I hereby declare that the work, which is being presented in the dissertation entitled "ADVANCED TURBULENCE MODELLING AND SIMULATION IN VARIOUS FLUID FLOW HEAT TRANSFER AND SURFACE CHEMISTRY PHENOMENA" towards the partial fulfillment of the requirement for the award of the degree of **Master of Technology in Chemical Engineering (Industrial Pollution Abatement)** submitted in the Department of Chemical Engineering, Indian Institute of Technology Roorkee, Roorkee (India) is an authentic record of my own work carried out during the period from July 2006 to June 2007, under the guidance of **Dr. C. B. Majumder, Assistant Professor, Department of Chemical Engineering, IIT Roorkee.**

I have not submitted the matter embodied in this dissertation for the award of any other degree or diploma.

Date: 28/06/07

Place: Roorkee

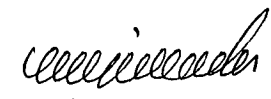

MAHARSHI SUBHASH

CERTIFICATE

This is to certify that the above statement made by the candidate is correct to the best of my knowledge and belief.

Date: 28/6/07

Place: Roorkee


Dr. C. B. MAJUMDER,
Assistant Professor,
Department of Chemical Engineering,
Indian Institute of Technology,
Roorkee – 247 667, INDIA

ACKNOWLEDGEMENT

I express my deep sense of gratitude to my guide **Dr. C.B. Majumder**, Assistant Professor, Department of Chemical Engineering, Indian Institute of Technology Roorkee, Roorkee, for his keen interest, constant guidance and encouragement throughout the course of this work, his experience, assiduity and deep insight of the subject held this work always on a smooth and steady course. Useful criticism and constant help extended in the hours of need had been immensely useful.

Thanks are due to **Dr. Shri Chand**, Professor and Head, Department of Chemical Engineering, Indian Institute of Technology Roorkee, Roorkee, for providing various facilities during this dissertation.

I thank all well wishers who in any manner directly or indirectly have put a helping hand in any part of this piece of work.

Above all, I want to express my heartiest gratitude to all my family members for their love, faith and support for me, which has always been a constant source of inspiration.

MAHARSHI SUBHASH

ABSTRACT

For first problem

Film cooling is a process that is used to protect turbine vanes in a gas turbine engine from exposure to hot combustion gases. In this paper, we have done the time-dependent analysis of film cooling by large-eddy-simulation (LES) model. We have obtained static-temperature contours, pressure contours, velocity vectors and temperature plot at $y = 12.7\text{mm}$ iso-surface at different time interval such as 10second, 20.37second and 40.74second. Significant results have been obtained.

For second problem

This work is the numerical analysis with the commercial CFD code Fluent 6.2. The purpose is to predict the stall condition for Axial-flow compressor. For this analysis NACA-2415 airfoil is used, as a blade profile. It is recommended that, this airfoil structure can also be used for the blade design of axial flow compressor. The study of flow over blade of compressor at four different angle of attack (AOA) i.e., 10° , 12.5° , 15° and 16° have been done. Lift-Drag Coefficients have been determined. Velocity vectors, Mach-number contours and pressure contours have been obtained. It has been found the stall angle at 12.5° . The velocity vectors and Dynamic pressure contours depicts nearly accurate result. The numerical results have been compared with the practical results, which has been carried out by NASA Langley Research Center, and found that the percentage error was less than $\pm 4\%$.

For third problem

In this work 3D CFD analysis of the Chemical Vapor Deposition Reactor (CVD) reactor has been done. The combined chemical and diffusion process has been taken into account for the formation of gallium and arsenic on the wafer. It has kept, the diffusion velocity; as constant and at different rotation of the wafer the optimum speed has been obtained at which the uniform deposition of the semiconductor materials could be obtained. We have done the analysis at 10rad/s, 20rad/s, 40rad/s, 70rad/s,

110rad/s and 120rad/s. It has been pointed out that at 120rad/s when diffusion velocity has kept constant at 0.02189m/s the uniform deposition has been achieved at the wafer surface.

CONTENTS

	Page No.
CANDIDATE'S DECLARATION	i
ACKNOWLEDGEMENT	ii
ABSTRACT	iii-iv
LIST OF TABLES	viii
LIST OF FIGURES	ix-xii
Chapter 1 INTRODUCTION	1-10
1.1 General	1-2
1.2 How does a CFD code work?	3-7
1.2.1 Pre-processor	3-4
1.2.2 Solver	4-7
1.2.2 (A) Finite difference methods	4
1.2.2 (B) Finite Element Method	5
1.2.2 (C) Spectral Methods	5
1.2.2 (D) The finite volume method	5-7
1.2.3 Post-processor	7
1.3 Advanced turbulence model	7-8
1.4 Introduction of problem	8-10
1.4.1 Turbine vane cooling analysis using LES turbulence model	8-9
1.4.2 Prediction of stall for axial flow compressor using Spalart-Allamaras model	9-10
1.4.3 Optimization of wafer rotation on deposition of gallium and arsenic in chemical vapor deposition reactor using CFD	10

Chapter 2	LITERATURE REVIEW	11-25
2.1	Turbine vane cooling analysis using LES turbulence model	11-15
2.2	Prediction of stall for axial flow compressor using Spalart-Allmaras model	16-20
2.3	Optimization of wafer rotation on deposition of gallium and arsenic in chemical vapor deposition reactor using CFD	21-25
2.4	Motivation of work	25
Chapter 3	PROBLEM DESCRIPTION	26-30
3.1	First Problem Description	26-27
3.2	Second Problem Description	27-28
3.2.1	NACA2415 Airfoil	27-28
3.2.2	Flow field	28
3.3	Third Problem Description	29-30
Chapter 4	MATHEMATICAL MODELING AND METHODOLOGY	31-45
4.1	First Problem	31-36
4.1.1	Governing Equations	31-33
4.1.2	Flow Solver	33-36
4.1.2 (A)	Conservation Form	33-34
4.1.2 (B)	Momentum Equations	34-35
4.1.2 (C)	Pressure Coupling	35-36
4.2	Second Problem	36-40
4.2.1	Transport Equation for the Spalart-Allmaras Model	36
4.2.2	Modeling of the Turbulent Viscosity	36
4.2.3	Modeling of the Turbulent Production	37-38
4.2.4	Modeling of the Turbulent Destruction	38
4.3	Solution method adopted in FLUENT 6.2	38-40
4.3.1	Boundary Conditions	39-40
4.3.2	Solution initialization	40

4.3.3 Solution	40
4.4 Third problem	41-45
4.4.1 The Laminar Finite-Rate Model	42-43
4.4.2 Boundary conditions and material properties	43-45
Chapter 5 RESULTS AND DISCUSSION	46-68
5.1 First Problem	46-51
5.2 Second Problem	51-58
5.3 Third Problem	59-68
Chapter 6 CONCLUSIONS AND FUTURE SCOPE OF THE WORK	69-70
6.1 Conclusions	69
6.2 Future scope of the work	70
REFERENCES	71-75
List of publications	76

Fig. No.	Title	Page No.
Figure 5.12	Static temperature profile at Iso-surface $y=12.74\text{mm}$ (0.5in) after 40.74sec	49
Figure 5.13	Grid generation around airfoil	52
Figure 5.14	Lift-coefficient at 10° AOA	53
Figure 5.15	Lift-coefficient at 12.5° AOA	53
Figure 5.16	Lift-coefficient at 15° AOA	53
Figure 5.17	Lift-coefficient at 16° AOA	54
Figure 5.18	Drag-coefficient at 10° AOA	54
Figure 5.19	Drag-coefficient at 12.5° AOA	54
Figure 5.20	Drag-coefficient at 15° AOA	55
Figure 5.21	Drag- coefficient at 16° AOA	55
Figure 5.22	Velocity Vectors at 10° AOA	55
Figure 5.23	Velocity Vectors at 12.5° AOA	56
Figure 5.24	Velocity Vectors at 15° AOA	56
Figure 5.25	Velocity Vectors at 16° AOA	56
Figure 5.26	pressure contours at 10° AOA	57
Figure 5.27	pressure contours at 12.5° AOA	57
Figure 5.28	pressure contours at 15° AOA	57
Figure 5.29	Dynamic pressure contours at 16° AOA	58
Figure 5.30	Stall Angle for NACA-2415 airfoil	58
Figure 5.31	Contours of gallium deposition rate 10rad/s	60

Fig. No.	Title	Page No.
Figure 5.48	Contours of arsenic deposition rate at 110rad/s	66
Figure 5.49	Plot of gallium deposition from center to right of the wafer at 110rad/s	66
Figure 5.50	Plot of arsenic deposition from center to right of the wafer at 110rad/s	67
Figure 5.51	Contours of gallium deposition rate at 120rad/s	67
Figure 5.52	Contours of arsenic deposition rate at 120rad/s	67
Figure 5.53	Plot of gallium deposition from center to right of the wafer at 120rad/s	68
Figure 5.54	Plot of arsenic deposition from center to right of the wafer at 120rad/s	68

INTRODUCTION

1.1 General

Computational Fluid Dynamics or CFD is the analysis of systems involving fluid flow, heat transfer and associated phenomena such as chemical reactions by means of computer-based simulation. The technique is very powerful and spans a wide range of industrial and non-industrial application areas. Some examples are:

- Aerodynamics of aircraft and vehicles: lift and drag
- Hydrodynamics of ships
- Power plant: combustion in IC engines and gas turbines
- Turbo-machinery: flows inside rotating passages, diffusers etc.
- Electrical and electronic engineering: cooling of equipment including micro-circuits
- Chemical process engineering: mixing and separation, polymer moulding
- External and internal environment of buildings: wind loading and heating/ventilation
- Marine engineering: loads on off-shore structures
- Environmental engineering: distribution of pollutants and effluents
- Hydrology and oceanography: flows in rivers, estuaries, oceans
- Meteorology: weather prediction
- Biomedical engineering: blood flows through arteries and veins

From the 1960s onwards the aerospace industry has integrated CFD techniques into the design, R&D and manufacture of aircraft and jet engines. More recently the methods have been applied to the design of internal combustion engines, combustion chambers of gas turbines and furnaces. Furthermore, motor vehicle manufacturers now routinely predict drag forces, under-bonnet air flows and the in-car environment with CFD. Increasingly CFD is becoming a vital component in the design of industrial products and processes.

The ultimate aim of developments in the CFD field is to provide a capability comparable to other CAE (Computer-Aided Engineering) tools such as stress analysis codes. The main reason why CFD has lagged behind is the tremendous complexity of the underlying

behavior, which precludes a description of fluid flows that is at the same time economical and sufficiently complete. The availability of affordable high performance computing hardware and the introduction of user- friendly interfaces have led to a recent upsurge of interest and CFD is poised to make an entry into the wider industrial community in the 1990s.

It is estimated the minimum cost of suitable hardware to be between £5000 and £10000 (plus annual maintenance costs). The perpetual license fee for commercial software typically ranges from £10000 to £50000 depending on the number of 'added extras' required. CFD software houses can usually arrange annual licenses as an alternative. Clearly the investment costs of a CFD capability are not small, but the total expense is not normally as great as that of a high quality experimental facility.

Moreover, there are several unique advantages of CFD over experiment-based approaches to fluid systems design:

- Substantial reduction of lead times and costs of new designs
- Ability to study systems where controlled experiments are difficult or impossible to perform (e.g. very large systems)
- Ability to study systems under hazardous conditions at and beyond their normal performance limits (e.g. safety studies and accident scenarios)
- Practically unlimited level of detail of results

The variable cost of an experiment, in terms of facility hire and/or man-hour costs, is proportional to the number of data points and the number of configurations tested. In contrast CFD codes can produce extremely large volumes of results at virtually no added expense and it is very cheap to perform parametric studies, for instance to optimize equipment performance.

In addition to a substantial investment outlay, an organization needs qualified people to run the codes and communicate their results and briefly consider the modeling skills required by CFD users.

1.2 How does a CFD code work?

CFD codes are structured around the numerical algorithms that can tackle fluid flow problems. In order to provide easy access to their solving power all commercial CFD packages include sophisticated user interfaces to input problem parameters and to examine the results. Hence all codes contain three main elements:

- (i) A pre-processor,
- (ii) A solver and
- (iii) A post-processor.

1.2.1 Pre-processor

Pre-processing consists of the input of a flow problem to a CFD program by means of an operator-friendly interface and the subsequent transformation of this input into a form suitable for use by the solver. The user activities at the pre-processing stage involve:

- Definition of the geometry of the region of interest: the computational domain.
- Grid generation-the sub-division of the domain into a number of smaller, non-overlapping sub-domains: a grid (or mesh) of cells (or control volumes or elements).
- Selection of the physical and chemical phenomena that need to be modeled.
- Definition of fluid properties.
- Specification of appropriate boundary conditions at cells which coincide with or touch the domain boundary.

The solution to a flow problem (velocity, pressure, temperature etc.) is defined at nodes inside each cell. The accuracy of a CFD solution is governed by the number of cells in the grid. In general, the larger the number of cells the better the solution accuracy. Both the accuracy of a solution and its cost in terms of necessary computer hardware and calculation time are dependent on the fineness of the grid. Optimal meshes are often non-uniform: finer in areas where large variations occur from point to point and coarser in regions with relatively little change. Efforts are under way to develop CFD codes with a (self-adaptive meshing capability. Ultimately such programs will automatically refine the grid in areas of rapid variations. A substantial amount of basic development work still needs to be done before these techniques are robust enough to be incorporated into

commercial CFD codes. At present it is still up to the skills of the CFD user to design a grid that is a suitable compromise between desired accuracy and solution cost. Over 50% of the time spent in industry on a CFD project is devoted to the definition of the domain geometry and grid generation. In order to maximize productivity of CFD personnel all the major codes now include their own CAD-style interface and/or facilities to import data from proprietary surface modelers and mesh generators such as PATRAN and I-DEAS. Up-to-date pre-processors also give the user access to libraries of material properties for common fluids and a facility to invoke special physical and chemical process models (e.g. turbulence models, radiative heat transfer, combustion models) alongside the main fluid flow equations.

1.2.2 Solver

There are three distinct streams of numerical solution techniques: finite difference, finite element and spectral methods. In outline the numerical methods that form the basis of the solver perform the following steps:

- Approximation of the unknown flow variables by means of simple functions.
- Discretisation by substitution of the approximations into the governing flow equations and subsequent mathematical manipulations.
- Solution of the algebraic equations.

The main differences between the three separate streams are associated with the way in which the flow variables are approximated and with the discretisation processes.

1.2.2 (A) Finite difference methods

Finite difference methods describe the unknowns ϕ of the flow problem by means of point samples at the node points of a grid of co-ordinate lines. Truncated Taylor series expansions are often used to generate finite difference approximations of derivatives of ϕ in terms of point samples of ϕ at each grid point and its immediate neighbours. Those derivatives appearing in the governing equations are replaced by finite differences yielding an algebraic equation for the values of ϕ at each grid point. Smith (1985) gives a comprehensive account of all aspects of the finite difference method.

1.2.2 (B) Finite Element Method

Finite element methods use simple piecewise functions (e.g. linear or quadratic) valid on elements to describe the local variations of unknown flow variables ϕ . The governing equation is precisely satisfied by the exact solution ϕ . If the piecewise approximating functions for ϕ are substituted into the equation it will not hold exactly and a residual is defined to measure the errors. Next the residuals (and hence the errors) are minimized in some sense by multiplying them by a set of weighting functions and integrating. As a result we obtain a set of algebraic equations for the unknown coefficients of the approximating functions. The theory of finite elements has been developed initially for structural stress analysis. A standard work for fluids applications is Zienkiewicz and Taylor (1991).

1.2.2 (C) Spectral Methods

Spectral methods approximate the unknowns by means of truncated Fourier series or series of Chebyshev polynomials. Unlike the finite difference or finite element approach the approximations are not local but valid throughout the entire computational domain. Again we replace the unknowns in the governing equation by the truncated series. The constraint that leads to the algebraic equations for the coefficients of the Fourier or Chebyshev series is provided by a weighted residuals concept similar to the finite element method or by making the approximate function coincide with the exact solution at a number of grid points. Further information on this specialized method can be found in Gottlieb and Orszag (1977).

1.2.2 (D) The finite volume method

The finite volume method was originally developed as a special finite difference formulation. It is central to four of the five main commercially available CFD codes: PHOENICS, FLUENT, FLOW3D and STAR-CD. The numerical algorithm consists of the following steps:

- Formal integration of the governing equations of fluid flow over all the (finite) control volumes of the solution domain.

- Discretisation involves the substitution of a variety of finite-difference-type approximations for the terms in the integrated equation representing flow processes such as convection, diffusion and sources. This converts the integral equations into a system of algebraic equations.
- Solution of the algebraic equations by an iterative method.

The first step, the control volume integration, distinguishes the finite volume method from all other CFD techniques. The resulting statements express the (exact) conservation of relevant properties for each finite size cell. This clear relationship between the numerical algorithm and the underlying physical conservation principle forms one of the main attractions of the finite volume method and makes its concepts much more simple to understand by engineers than finite element and spectral methods. The conservation of a general flow variable ϕ , for example a velocity component or enthalpy, within a finite control volume can be expressed as a balance

$$\left[\begin{array}{l} \text{Rate of change of} \\ \phi \text{ in the control} \\ \text{volume with respect to time} \end{array} \right] = \left[\begin{array}{l} \text{Net flux of } \phi \\ \text{du to convection into} \\ \text{the control volume} \end{array} \right] + \left[\begin{array}{l} \text{Net flux of } \phi \\ \text{due to diffusion into} \\ \text{the control volume} \end{array} \right] + \left[\begin{array}{l} \text{Net rate of creation} \\ \text{of } \phi \text{ inside the} \\ \text{control volume} \end{array} \right]$$

CFD codes contain discretisation techniques suitable for the treatment of the key transport phenomena, convection (transport due to fluid flow) and diffusion (transport due to variations of ϕ from point to point) as well as for the source terms (associated with the creation or destruction of ϕ) and the rate of change with respect to time. The underlying physical phenomena are complex and non-linear so an iterative solution approach is required. The most popular solution procedures are the TDMA line-by-line solver of the algebraic equations and the SIMPLE algorithm to ensure correct linkage between pressure and velocity. Commercial codes may also give the user a selection of further, more recent, techniques such as Stone's algorithm and conjugate gradient methods.

1.2.3 Post-processor

As in pre-processing a huge amount of development work has recently taken place in the post-processing field. Owing to the increased popularity of engineering workstations, many of which have outstanding graphics capabilities, the leading CFD packages are now equipped with versatile data visualization tools. These include:

- Domain geometry and grid display
- Vector plots
- Line and shaded contour plots
- 2D and 3D surface plots
- Particle tracking
- View manipulation (translation, rotation, scaling etc.)
- Color postscript output

More recently these facilities may also include animation for dynamic result display and in addition to graphics all codes produce trustworthy alphanumeric output and have data export facilities for further manipulation external to the code. As in many other branches of CAE the graphics output capabilities of CFD codes have revolutionized the communication of ideas to the non-specialist.

1.3 Advanced turbulence model

Large- Eddy Simulation

Detached- Eddy Simulation, Roy et al (2003)

Direct Numerical Simulation, Azzi et al (2007)

Spalart- Allmaras Model

In this dissertation, Large- Eddy Simulation (LES), Spalart-Allmaras (S-A) model and surface chemistry phenomena for three different problems have been solved.

The LES model has been employed in the film cooling, S-A model in the compressible flow and Surface chemistry in the thin film deposition on the wafer in Chemical Vapor Deposition (CVD) reactor.

1.4 Introduction of problem

The introductions of all three problems have been given below

1.4.1 Turbine vane cooling analysis using LES turbulence model

The time-dependent solution of turbulent flow is computationally extremely intensive. In a direct numerical simulation (DNS) essentially all scales present in the flow field are solved. Due to the need of huge computational resources, DNS is usually applied with a relatively low Reynolds number in basic flows such as a channel flow. Spectral methods are often utilized because they reduce the number of the grid points needed due to their accuracy. The application of spectral methods in complex domains is difficult which makes them less appealing as engineering tools. In a large-eddy simulation (LES) the small-scale motion is not solved which reduces the computational cost. The effect of the small-scale motion is usually modeled with a sub-grid-scale model (SGS-model). As the computational power has increased, the applications in engineering have become feasible. Therefore, low-order finite-difference solutions in LES have recently become popular, as shown in Breuer (1998) and Bui (2000) to name just two. In this problem, the system that is modeled consists of three parts: a duct, a hole array and a plenum. The duct is modeled with a hexahedral mesh, and the plenum and hole regions are modeled using a tetrahedral mesh. These two meshes are merged together to form a hybrid mesh, with a non-conformal interface boundary between them.

Due to symmetry of the hole array, only a portion of the geometry is modeled in FLUENT, with symmetry applied to the outer boundaries. The duct contains a high-velocity fluid in stream wise flow (Figure 1.1). An array of holes intersects the duct at an inclined angle and a cooler fluid is injected into the holes from a plenum. The coolant that moves through the holes acts to cool the surface of the duct, downstream of the

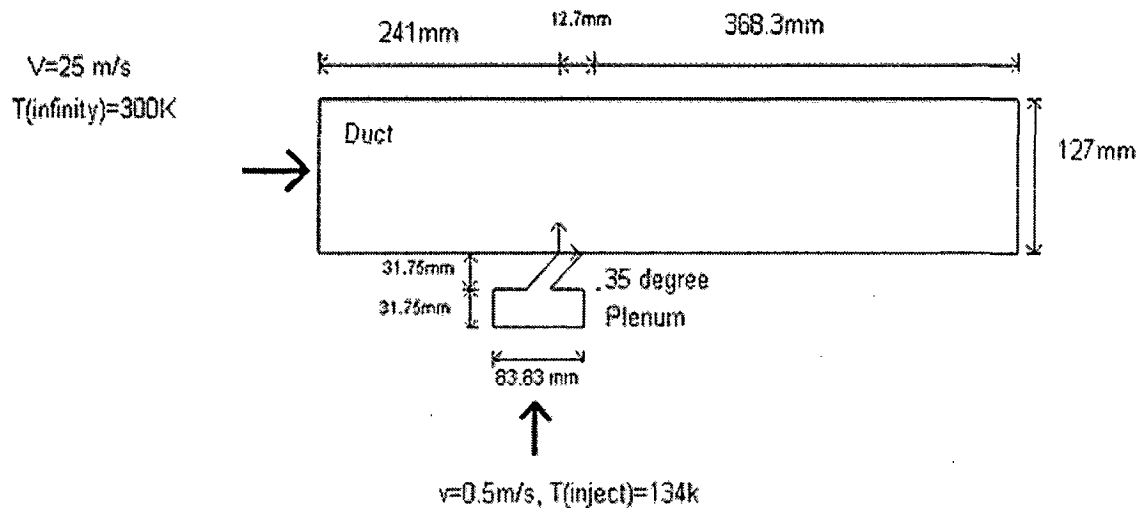


Figure 1.1. Schematic of the Problem, Front view

injection. Both fluids are air, and the flow is classified as turbulent. The velocity and temperature of the stream wise and cross-flow fluids are known, and FLUENT is used to predict the flow and temperature fields that result from convective heat transfer.

1.4.2 Prediction of stall for axial flow compressor using Spalart-Allmaras model

Stalling of a stage of axial flow compressor is defined as aerodynamic stall or the breakaway of the flow from the suction side of the blade aerofoil.

Many researchers have studied the operation of single stage fans and compressors at flow coefficients low enough to cause stalling. The most detailed survey of various types of stalling has been given by Smith and Fletcher (1954). Their results have been summarized as follows:

A rotating stall which may rotate in the opposite direction of the compressor at approximately one-half the compressor rotational speed. Such a stall cell may include a region of very small through velocity or even reversed flow. In other words, the phenomenon of reduction in lift force at higher angle of attack is known as stalling. Several theories have been developed by Marbel et al (1954), Sears (1953) and Stenning et al (1956) for linear analysis of the rotating stall in axial- flow compressors.

Here, I have done CFD analysis of this stalling phenomenon, and chosen for this analysis NACA2415 airfoil as blade profile.

1.4.3 Optimization of wafer rotation on deposition of gallium and arsenic in chemical vapor deposition reactor using CFD

Chemical Vapor Deposition (CVD) has been an important technology in microelectronics industry for producing thin solid films on heated wafers. The essential mechanisms underlying CVD processes are chemical reactions in the gas phase and on surfaces, combined with mass, momentum and energy transport. The interactions of chemical and transport processes influence the quality of the deposited films.

In the present work, the CFD analysis has been done so that it could contribute in significant way in the CVD reactor design. The CFD analysis provides an excellent economic alternative to trial-and-error based experimental techniques. Investigation of various operating parameters to the properties of deposited film has been done by Chai et al (1999), Kommu et al (2000) and Barathieu et al (2001).

Evolutionary Algorithm (EA) has been used by Cho and Choi (2000), Grujicic et al (2002) and Itle et al (2004); they have modeled the gas flow, heat and mass-transfer phenomena and optimized the uniform growth rate deposited material on wafers. A previous combined experimental/computational analysis of the CVD reactor has resulted in the preliminary detection of the origins of the spatial variation of the growth rate across the wafer at various rotation speeds by Xenidou et al (2004).

LITERATURE REVIEW

2.1 Turbine vane cooling analysis using LES turbulence model

Kapadia et al (2003) has explored the possibility of detached eddy simulation (DES) for the film cooled flat plate. A geometry of single row of 35 degree round holes on a flat plate is used for the blowing ratio of 1.0 and density ratio of 0.5. Use of symmetry boundary condition is avoided to capture three dimensional, unsteady, turbulent nature of the flow. Present simulation uses unstructured grid and parallel algorithm to perform DES. Implicit time -stepping is used for the CFL number up to one million. Presence of asymmetry in the DES solution is documented by plotting the temperature and velocity profiles at various stream-wise locations. Numerical calculation of effectiveness is validated with reported experimental results.

The complex dynamic nature of the span wise vortices in film cooling of turbine blades makes it necessary to accurately model the flow field temporally and spatially using detailed simulation techniques like direct numerical simulation or large eddy simulation of turbulence. Although, the later requires less computational effort and thus can simulate flows at higher Reynolds number than direct simulation, both these methods remain very expensive. As a viable alternative accomplished by Roy et al (2003), Spalart-Allamaras based detached eddy simulation (DES) that has been applied to a film cooled flat plate for the first time. The numerical model uses an unstructured grid system to resolve the dynamic flow structures on both sides of the plate as well as inside the hole itself. Detailed computation of a single row of 35 degree round holes on a flat plate has been obtained for blowing ratio of 1.0, and a density ratio of 2.0. The DES solution is also benchmarked with Reynolds averaged Navier-Stokes formulation for the same blade-hole configuration. The comparison shows that the DES simulation, which makes no assumption of isotropy downstream of the hole, greatly enhances the realistic description of the dynamic mixing processes.

A three-dimensional Navier–Stokes simulation has been performed by Heidmann et al (2000), for a realistic film cooled turbine vane using the LeRC-HT code. The simulation includes the flow regions inside the coolant plena and film cooling holes in addition to the external flow. The vane is the subject of an upcoming NASA Lewis Research Center experiment and has both circular cross-sectional and shaped film cooling holes. This complex geometry is modeled using a multi block grid, which accurately discretizes the actual vane geometry including shaped holes. The simulation matches operating conditions for the planned experiment and assumes periodicity in the span-wise direction on the scale of one pitch of the film cooling hole pattern. Two computations were performed for different isothermal wall temperatures, allowing independent determination of heat transfer coefficients and film effectiveness values. The results indicate separate localized regions of high heat flux in the showerhead region due to low film effectiveness and high heat transfer coefficient values, while the shaped holes provide a reduction in heat flux through both parameters. Hole exit data indicate rather simple skewed profiles for the round holes, but complex profiles for the shaped holes with mass fluxes skewed strongly toward their leading edges.

Azzi et al (2003) has reported a numerical modeling and simulation studies of film cooling from stream-wise injection holes with various small hole length to diameter ratios, using a standard $k-\varepsilon$ turbulence model with wall function. An anisotropic model was also applied in order to correct the deficit in lateral spreading of the $k-\varepsilon$ model. Comparisons of the present predicted results with experimental data and numerical results of previous studies show that using anisotropic turbulence model, multi-block grid techniques and extending the computational domain into the plenum supply of the injection holes tend to improve the prediction of the film cooling effectiveness especially at low blowing rates while for high blowing rates a more detailed description than the wall law approach is needed to describe the lift-off of the jet. Moreover, the film cooling protection is reduced as the hole L/d ratio is decreased.

Gauntner (1977) has searched, Film ejection from discrete holes in the suction surface of a turbine vane was studied for hole axes slanted 30degree to the surface in the stream-wise direction and slanted 30 degree to the surface and 45 degree from the stream-

wise direction toward the hub. The holes were near the throat are in a five- row, staggered array with 8-diameter spacing. The mass flux ratios were as high as 1.2. The data were obtained in an annular sector cascade at conditions where both the ratio of the boundary-layer-momentum-thickness to-hole diameter and the momentum-thickness Reynolds number were typical of an advanced turbofan engine at takeoff. Wall temperatures were measured downstream of each of the rows of holes. The data show that the cooling effectiveness for compound-angle injection is greater than that of slanted in-line injection for mass flux ratios as high as 1.2; the cooling effectiveness for slanted in-line injection reaches a local maximum at a mass flux ratio of about 0.5 and then decreases for greater mass flux ratios for injection into an adverse pressure gradient; and the cooling effectiveness for compound-angle injection reaches a local maximum at a mass flux ratio of about 0.5 and then resumes increasing at a mass flux ratio of about 0.7. The last two results are consistent with the implications of flow visualization results of a referenced study in which film ejected from slanted in-line holes separates from the surface at a mass flux ratio of about 0.5 and film ejected from compound-angle holes remains close to the surface even at high mass-flux ratios. Also included is a closed-form analytical solution for temperature within a film cooled wall. The solution is subject to three homogeneous and one non-homogeneous boundary condition.

Predictions of turbine blade film cooling have traditionally employed Reynolds-averaged Navier-Stokes solvers and two-equation models for turbulence. Evaluation of several versions of such models have revealed that the existing two-equation models fail to resolve the anisotropy and the dynamics of the highly complex flow field created by the jet-cross-flow interaction. A more accurate prediction of the flow field can be obtained from large eddy simulations (LES) where the dynamics of the larger scales in the flow are directly resolved. Tyagi et al (2003) have used that approach, and results are presented for a row of inclined cylindrical holes at blowing ratios of 0.5 and 1 and Reynolds numbers of 11,100 and 22,200, respectively, based on the jet velocity and hole diameter. Comparison of the time-averaged LES predictions with the flow measurements shows that LES is able to predict the flow field with reasonable accuracy. The unsteady three-dimensional flow field is shown to be dominated by packets of hairpin-shaped

vortices. The dynamics of the hairpin vortices in the wake region of the injected jet and their influence on the unsteady wall heat transfer are presented. Generation of “hot spots” and their migration on the film-cooled surface are associated with the entrainment induced by the hairpin structures. Several geometric properties of a “mixing interface” around hairpin coherent structures are presented to illustrate and quantify their impact on the entrainment rates and mixing processes in the wake region.

Roy et al (1998) has studied the thermal effect of cool jets issuing into an incompressible hot cross flow at an angle over a turbine blade. Numerical solutions using the turbulence closure model for eight multiple hole arrangements with three different hole spacing and three different jet issuing angles document strong to moderate secondary vortex structures spanning normal to the direction of the jet. This fully three dimensional flow field strongly influences the cooling performance of the hole-blade system. For a generalized body-fitted three dimensional finite element model, computational results suggest an optimum hole spacing and low issuing angle for maximum cooling efficiency.

Azzi et al (2007) have done numerical prediction of a new 3D film cooling hole geometry, the converging slot-hole or console. The console geometry is designed in order to improve the heat transfer and aerodynamic loss performance of turbine vane and rotor blade cooling systems without losing the mechanical strength of a row of discrete holes. The cross section of the console changes from a circular shape at the inlet to a slot at the exit. Previous successful application of a new anisotropic DNS based two-layer turbulence model to cylindrical and shaped hole injections is extended to predict film cooling for the new console geometry. The suitability of the proposed turbulence model for film cooling flow is validated by comparing the computed and the measured wall-temperature distributions of cylindrical hole injections. The result shows that the anisotropic eddy-viscosity/diffusivity model can correctly predict the span-wise spreading of the temperature field and reduce the strength of the secondary vortices. Comparative computations of the adiabatic film cooling effectiveness associated with the three geometries tested in the present study (cylindrical, shaped, and console) show that the new console film-cooling hole geometry is definitely superior to the other geometries

as shown by the uniform lateral spreading of the effectiveness with a slight enhancement downstream of the intersection of the two consoles.

The velocity field of multiple jets-in-cross-flow has been examined experimentally for various jet hole supply plenum configurations using particle image velocimetry. The jet hydrodynamics are discussed in relation to implications on gas turbine film-cooling applications. The counter-flow plenum case produced desirable in-hole vortices of opposite rotational sense to that of the primary counter-rotating vortex pair (CRVP) in the jet. For this case, the interaction of in-hole vorticity and the CRVP weakened the CRVP, resulting in a lower trajectory and increased span-wise spreading. Peterson et al (2002) has found that this is advantageous for film-cooling applications where surface coverage and jet attachment are necessary to prevent hot-gas penetration to the blade or vane surface.

Sargison et al (2005) presented flow visualization experiments for a novel film-cooling hole, the converging slot-hole or console for short. Previously published experimental results have demonstrated that the console improved both the heat transfer and the aerodynamic performance of turbine vane and rotor blade cooling systems. Flow visualization data for a row of consoles were compared with that of cylindrical and fan-shaped holes and a slot at the same inclination angle of 35 degree to the surface, on a large-scale, flat-plate model at engine representative Reynolds numbers in a low speed tunnel with ambient temperature mainstream flow. In the first set of experiments, the flow was visualized by using a fine nylon mesh covered with thermo chromic liquid crystals, allowing the measurement of gas temperature contours in planes perpendicular to the flow. This data demonstrated that the console film was similar to a slot film, and remained thin and attached to the surface for the coolant-to-mainstream momentum flux ratios of 1.1 to 40 and for a case with no cross-flow (infinite momentum flux ratio). A second set of flow visualization experiments using water/dry-ice fog have confirmed these results and have shown that the flow through all coolant geometries is unsteady.

2.2 Prediction of stall for axial flow compressor using Spalart-Allmaras model

Barakos et al (2003) have investigated subsonic and transonic turbulent flows around oscillating and ramping aerofoils under dynamic-stall conditions. The investigation is based on a high resolution Godunov-type method and several turbulence closures. The Navier–Stokes and turbulence transport equations are solved in a strongly coupled fashion via an implicit-unfactored scheme. We present results from several computations of flows around oscillating and ramping aerofoils at various conditions in order to (i) assess the accuracy of different turbulence models and (ii) contribute towards a better understanding of dynamic-stall flows. The results show that the employed non-linear eddy viscosity model generally improves the accuracy of the computations compared to linear models, but at low incidence angles the Spalart–Allmaras one-equation model was found to provide adequate results. Further, the computations reveal strong similarities between laminar and high-Reynolds number dynamic stall flows as well as between ramping and oscillating aerofoil cases. Investigation of the Mach number effects on dynamic-stall reveals a delay of the stall angle within a range of Mach numbers. Investigation of the reduced frequency effects suggests the existence of an (almost) linear variation between pitch rate and stall angle, with higher slope at lower pitch rates. The pitch rate affects both the onset of dynamic-stall as well as the evolution of the associated vortical structures.

Numerical simulations of dynamic-stall phenomena have been performed by Barakos et al (2000) using an implicit unfactored Navier-Stokes solver and various turbulence closures, including linear and nonlinear low-Re eddy-viscosity models. The accuracy of the models has been assessed against a range of experimental data for ramping and oscillating aerofoils at subsonic and transonic conditions. The computations indicate that the nonlinear eddy-viscosity models better predict the shedding of the dynamic-stall vortex and the unsteady aerodynamic loads.

The propagation of strong distortion at inlet of an axial compressor is investigated by applying the critical distortion line and the integral method, Liu et al (2003). The practical applications, such as the inlet conditions of flaming of leakage fuel during mid-

air refueling process, are implemented to show the details of the numerical methodology used in analysis of the axial flow compressor behavior and the propagation of inlet distortion. From the viewpoint of compressor efficiency, the propagation of inlet flow distortion is further described by a compressor critical performance and its critical characteristic. The simulated results present a useful physical insight to the significant effects of inlet parameters on the distortion extension, velocity, and compressor characteristics. The distortion level, incidence angle and the size of distortion area at compressor inlet, and the rotor blade speed are found being the major parameters affecting the mass flow rate of engine.

Donald et al (1977) have worked on the performance of the first stage of a transonic, multistage compressor, designed at the NASA Lewis Research Center, was mapped over a range of inlet-guide-vane and stator-blade settings. Both stalled and stall-free performance data were obtained to provide a better understanding of the performance of this stage in the multistage environment, where difficulties were encountered in matching the stages. Tests were conducted at 60, 80, and 100 percent of design speed and flow was further reduced, a relatively sharp drop in pressure ratio occurred and was followed by a continuing but more gradual reduction in pressure ratio with reduced flow. Even though the pressure-ratio gradient at the stall line was steep, a discontinuity was not noted. The position of the stall line on the map of the total-pressure ratio against equivalent weight flow was essentially unchanged for the three inlet-guide vane and stator-blade settings. However, as the inlet guide vanes and stator blades were closed from their design settings, the stall points for the three speeds moved to lower flows and correspondingly lower pressure ratios. This partly explains the apparent ineffectiveness of inlet-guide-vane and stator-blade reset as a means of matching the stages of the five-stage compressor. Large changes in the inlet-guide-vane and stator. For the three inlet-guide-vane and stator-blade settings result in substantial reductions in stage efficiency.

The turbulence fluid flow ($Re = 2 \times 10^{06}$) around a two dimensional wing, NACA4412, on different angles of attack near and far from the ground for fixed and moving ground conditions with the RANS (Reynolds averaged Navier-stokes) equations is calculated. Realizable $k-\varepsilon$ turbulence model with Enhanced wall treatment and

Spalart-Allmaras model are used, by Firooz et al (2006). In order to validate the present numerical data the computational results for NACA 4412 in unbounded flow is compared with experimental data. The lift coefficient simulated by the moving bottom condition near the ground is greater than the fixed bottom condition, and far from the ground is vice versa, but the drag coefficient simulated by the moving bottom far from the ground is to some extent larger than that of the fixed one and near the ground is vice versa. Also it is concluded that on different angles of attack, lift coefficient of the airfoil, increases as it approaches the ground. In the moving ground condition the drag coefficient decreases as it approaches the ground, but in the fixed ground condition although the drag coefficient decreases far from the ground but it increases near the ground, as the airfoil approaches the ground.

Maalawi et al (2003) have categorized practical families of horizontal-axis wind turbine rotors, which are optimized to produce the largest possible power output. Refined blade geometry is obtained from the best approximation of the calculated theoretical optimum chord and twist distributions of the rotating blade. The mathematical formulation is based on dimensionless quantities so as to make the aerodynamic analysis valid for any arbitrary turbine models having different rotor sizes and operating at different wind regimes. The selected design parameters include the number of blades, type of airfoil section and the blade root offset from hub center. The effects of wind shear as well as tower shadow are also examined. A computer program has been developed to automate the overall analysis procedures, and several numerical examples are given showing the variation of the power and thrust coefficients with the design tip speed ratio for various rotor configurations.

Fares et al (2004) have introduced a complete and general one-equation model capable of correctly predicting a wide class of fundamental turbulent flows like boundary layer, wake, jet, and vortical flows. The starting point is the mature and validated two-equation $k-\omega$ turbulence model of Wilcox. The newly derived one-equation model has several advantages and yields better predictions than the Spalart-Allmaras model for jet and vortical flows while retaining the same efficiency and quality of the results for near-

wall turbulent flows without using a wall distance. The derivation and validation of the new model using findings computed by the Spalart–Allamaras and the $k-\omega$ models are presented and discussed for several free shear and wall-bounded flows.

An unsteady flow around a transversal circular cylinder has been analyzed by Isaev et al (2005), on the basis of solution of Navier–Stokes and Reynolds equations, using one- and two-parameter differential models of turbulence, by the implicit factorized method with the use of different-density structured and non-structured grids. Solvers of specialized multi-block and universal packages have been tested.

Sustained operation of airfoils at stalled flow conditions, which in the past has been demanded only of compressor and helicopter blades, is now a design requirement for advanced aircraft with super maneuverability. Thus, it has become a general requirement in the aerospace industry that the vehicle designer be able to assess what effects the separated flow will have, especially on vehicle dynamics, as these effects are often adverse and always of large magnitude relative to the attached flow aerodynamics. In spite of rapid development of computational means, purely theoretical methods for prediction of the effect of separated flow on rigid and elastic vehicle dynamics are not presently available, and will not be for some time. To compound the problem for the vehicle designer, dynamic simulation in an experiment requires the testing to be performed at full scale Reynolds number. Ericsson et al (1988) shows a practical solution to this dilemma. An analytic method is described that uses static experimental data to predict the separated flow effect on the incompressible unsteady aerodynamics. Key parameters in the analytic relationship between steady and non-steady aerodynamics are the following: (i) the time lag occurring before a change of flow conditions can affect the separation-induced aerodynamic loads; (ii) the accelerated flow effect, i.e. the pressure gradient lag relative to the static aerodynamic characteristics; (iii) the moving wall effect, i.e. the effect of the non-steady boundary condition at the vehicle surface. Using the existing experimental data-base an analytic theory is formulated that can predict the separation-induced unsteady aerodynamics if the static characteristics are known from theory or experiment.

The representation of loss in a cascade by the appearance of blockage has been extended to deal with blade rows by the use of a source distribution to represent this blockage, and in the case of the actuator disc approximation, the presence of sources is confined to an axi-symmetric distribution over the actuator disc. A-Daini et al (1979) have found that if a typical dependence of loss (and consequently diffusion ratio) upon incidence for each section of an axial compressor rotor is represented in this manner, the influence of blockage on the axial velocity distribution may be found using the potential equation combined with the usual actuator disc approximation. Study of the behavior of the controlling ordinary differential equation for the axial velocity ahead of the disc reveals that as the flow is reduced, the equation contains a singularity within the range of radius and a meaningful solution does not exist. This result is interpreted as the limit to continuous operation and reasonable agreement between this predicted limit and the appearance of abrupt stall (experimentally) is found.

The dynamic stall behavior of the supercritical NLR 7301 airfoil is analyzed by Weber et al (2000), with a 2-D thin-layer Navier-Stokes code. The code solves the compressible Reynolds-averaged Navier-Stokes equations with an upwind biased numerical scheme in combination with the Baldwin-Lomax; Baldwin and Lomax (1978), or the Baldwin-Barth; Baldwin and Barth (1990), turbulence models. The effect of boundary layer transition is incorporated using the transition length model of Gostelow et al (1996) The transition onset location is determined with Michel's formula or it can be specified as an input parameter. The two turbulence models yield significantly different steady-state lift coefficients at incidences greater than 83. The use of the one-equation Baldwin-Barth model together with the Gostelow transition model is found to give substantially better agreement with the experimental data of McCroskey et al (1982) than the Baldwin-Lomax model. Also, the unsteady computations are strongly affected by the choice of the turbulence model. The Baldwin-Barth model predicts the lift hysteresis loops consistently better than the algebraic turbulence model. However, the one-equation model improves the prediction of the moment hysteresis loops only for one test case.

2.3 Optimization of wafer rotation on deposition of gallium and arsenic in chemical vapor deposition reactor using CFD

Fluid flow, heat and mass transport processes in a two-dimensional converging channel with a heated susceptor are investigated by Khanafer et al (2005), numerically for various pertinent parameters. A model is developed to analyze the impact of the transport mechanisms on the deposition process of a typical chemical vapor deposition. Discretization of the governing equations is achieved using a finite element scheme based on the Galerkin method of weighted residuals. Comparisons with previously published work on the basis of special cases are performed and found to be in excellent agreement. Various results for the streamlines, isotherms, and iso-concentrations are presented and discussed for different parametric values. The results of the present investigation show that the tilted susceptor can produce a greater deposition and a more even distribution of material than a non-tilted susceptor. Moreover, the tilted susceptor is found to suppress the effect of transverse recirculation regions inside the reactor.

Three-dimensional (3-D) computational fluid dynamics (CFD) tools were applied to enhance capabilities of the two-dimensional (2-D) simulation in predicting such important characteristics of the SiC Chemical Vapor Deposition (CVD) epitaxial growth process as growth rate, growth rate non-homogeneity in longitudinal and transverse directions, and growth morphology. Depletion of the precursors in the gas phase along the growth direction was shown by Koshka et al (2003), to be one of the most important sources for the growth rate nonhomogeneity. The rate of precursor depletion along the growth direction in the center of the susceptor is different from that closer to the sides of the susceptor due to the non-homogeneous temperature profile in the transverse direction. This difference causes a significant increase in the growth rate away from the center of the susceptor toward the reactor walls. Simulated precursor super saturation above the growth surface was the highest at the leading edge of the susceptor and near the reactor walls, which correlates with the morphology degradation in those regions.

Asmann (2001) et al have studied effects of substrate rotation on the chemical vapor deposition (CVD) of diamond is investigated utilizing a Triple Torch Plasma

Reactor (TTPR) activation source. Diamond deposition experiments are conducted with an Ar-H₂-CH₄ plasma gas mixture at reduced pressures. Substrate rotation is achieved by means of a variable speed DC gear motor used to rotate the substrate shaft. Rotation of the substrate during deposition, as well as rotation and offsetting the substrate axis from the converging plasma-jet axis, is found to increase the average mass deposition rate as well as the average area of deposit when compared to a stationary substrate. Film and crystal size uniformity of the deposit are found to be enhanced, and deposit roughness decreased by rotating, and rotating plus offsetting the substrate when compared to a stationary substrate. Rotational speed and offsetting the substrate results in negligible differences compared to pure axial rotation. The effect of rotation on substrate temperature is believed to be more significant than the effect of substrate rotation on plasma fluid dynamics.

Steady and transient mass transport phenomena within an inverted, stagnation flow, cold-wall CVD reactor were investigated by observing the concentration of a tracer species (CH₄) with in situ Raman spectroscopy, Hwang et al (2005). The transient studies revealed that the use of matched reactor inlet velocities is crucial to minimize recirculating flow patterns and that the magnitude of the gas velocity is also important in gas switching. In the steady-state studies, it was observed that the existence of a sufficiently large density gradient in the reactor initiates natural convection and under some conditions introduces flow instability and thus three-dimensional (3-D) flows. The onset of instability was characterized by solutal density difference, gas velocity, and distance traveled by the gas. A steady-state, 2-D axi-symmetric reactor model validated with experimental data was used to analyze the measured tracer concentration profiles.

Kim et al (2005) have studied a vertical thermal radio frequency (RF)-PECVD reactor is modeled to investigate thermal flow and the deposition rates with various shapes of the showerhead. The showerhead in the chemical vapor deposition (CVD) reactor has the shape of a ring and gases are injected in parallel with the susceptor, which is a rotating disk. In order to achieve the high deposition rates, we have simulated the thermal flow fields in the reactor with several showerhead models. Especially the effects of the number of injection holes and the rotating speed of the susceptor are studied. Using

a commercial code, CFD-ACE, which uses finite-volume method (FVM) and SIMPLE algorithm, governing equations have been solved for the pressure, mass-flow rates and temperature distributions in the CVD reactor. With the help of the Nusselt number and Sherwood number, the heat and mass transfers on the susceptor are investigated.

Ern et al (1996) have investigated computationally a metalorganic chemical vapor deposition reactor. Our model combines a three-dimensional solution of the coupled Navier-Stokes/energy equations in a vorticity-velocity form, new and accurate multi-component transport algorithms, and detailed finite rate chemistry in the gas phase and on the crystal surface. They have applied a modified Newton method along with efficient Jacobian evaluation and linear algebra procedures in order to obtain a numerical solution. The present study focuses primarily on film uniformity and carbon incorporation levels. Their numerical results show the critical importance of transport modeling for an accurate description of the growth process. Furthermore, three growth regimes arise as a function of susceptor temperature: a kinetics-controlled regime at low temperatures, a diffusion-controlled regime at intermediate temperatures, and a desorption-controlled regime at high temperatures. These results are further supported by a sensitivity analysis with respect to both gas phase and surface chemistry.

Bliss et al (2006) have worked on the method for growing thick epitaxial layers of GaAs on orientation-patterned wafers by low-pressure hydride vapor phase epitaxy is described. For nonlinear optical applications, it is necessary to grow very thick gratings to accommodate the pump laser as it enters through the side and propagates across the patterned layer. The low-pressure method allows for rapid growth at rates well above 100 mm/h on wafers with patterned stripes having 30–500 μm widths. Parasitic deposition of GaAs on the reactor walls upstream of the sample can reduce the growth rate significantly after a few hours. Various techniques are described for eliminating the parasitic growth. Layers over 500 μm thick have been successfully produced during 8 h of growth.

Ern et al (1997) have worked on the numerical model of a three-dimensional, horizontal channel; chemical vapor deposition reactor is presented in order to study gallium arsenide growth from tri-methyl-gallium and arsine source reactants. Fluid flow and temperature predictions inside the reactor are obtained using the vorticity-velocity form of the three-dimensional, steady-state Navier–Stokes equations coupled with a detailed energy balance equation inside the reactor and on its walls. Detailed gas phase and surface chemistry mechanisms are used to predict the chemical species profiles inside the reactor, the growth rate distribution on the substrate, and the level of carbon incorporation into the grown layer. The species diffusion velocities are written using the recent theory of iterative transport algorithms and account for both thermal diffusion and multi-component diffusion processes. The influence of susceptor temperature and inlet composition on growth rate and carbon incorporation is found to agree well with previous numerical and experimental work.

Wilson et al (2002) have design and optimized the Chemical Vapor Deposition (CVD) systems for material fabrication. Design and optimization of the CVD process is necessary to satisfying strong global demand and ever increasing quality requirements for thin film production. Advantages of computer aided optimization include high design turnaround time, flexibility to explore a larger design space and the development and adaptation of automation techniques for design and optimization. A CVD reactor consisting of a vertical impinging jet at atmospheric pressure, for growing titanium nitride films, is studied for thin film deposition. Numerical modeling and simulation are used to determine the rate of deposition and film uniformity over a wide range of design variables and operating conditions. These results are used for system design and optimization. The optimization procedure employs an objective function characterizing film quality, productivity and operational costs based on reactor gas flow rate, susceptor temperature and precursor concentration. Parameter space mappings are used to determine the design space, while a minimization algorithm, such as the steepest descent method, is used to determine optimal operating conditions for the system. The main features of computer aided design and optimization, using these techniques, are discussed in detail.

Bouteville (2005) has given an overview of the different applications of the numerical simulation in chemical vapor deposition (CVD) process and equipment. In particular, emphasis will be given to the modeling of Rapid Thermal Low Pressure CVD and to the perspective of modeling Spray CVD.

2.4 Motivation of work

The solution of film cooling using LES model has not been obtained. Although, it requires less computational cost than that of DES model.

For investigation of the applicability of LES model was also the reason.

For second problem, the stall is the general trouble in the axial flow compressor. Other reason, how best suited Spalart- Allamaras model for compressible flow solves the simulation in the prediction of the stall.

For surface chemistry phenomena, the thin film deposition has been modeled. The all complexity of the problem has been included. The optimization of the wafer has been done. It further, helps in the design of the CVD reactor for thin coatings of micro-electronics equipments.

PROBLEM DESCRIPTION

3.1 First Problem Description

This problem considers a model of a 3D section of a film cooling test rig. A schematic is shown in Figures 3.1 and 3.2. The problem consists of a duct, 622 mm long, with cross sectional dimensions of 19 mm \times 127 mm.

An array of uniformly spaced holes is located at the bottom of the duct. Each hole has a diameter of 12.7 mm, is inclined at 35° and is spaced 38.2 mm apart laterally. Cooler injected air enters the system through the plenum, with cross-sectional dimensions of 83.83 mm \times 31.75 mm. Because of the symmetry of the geometry, only a portion of the domain needs to be modeled. The computational domain is shown in outline in Figure 3.2.

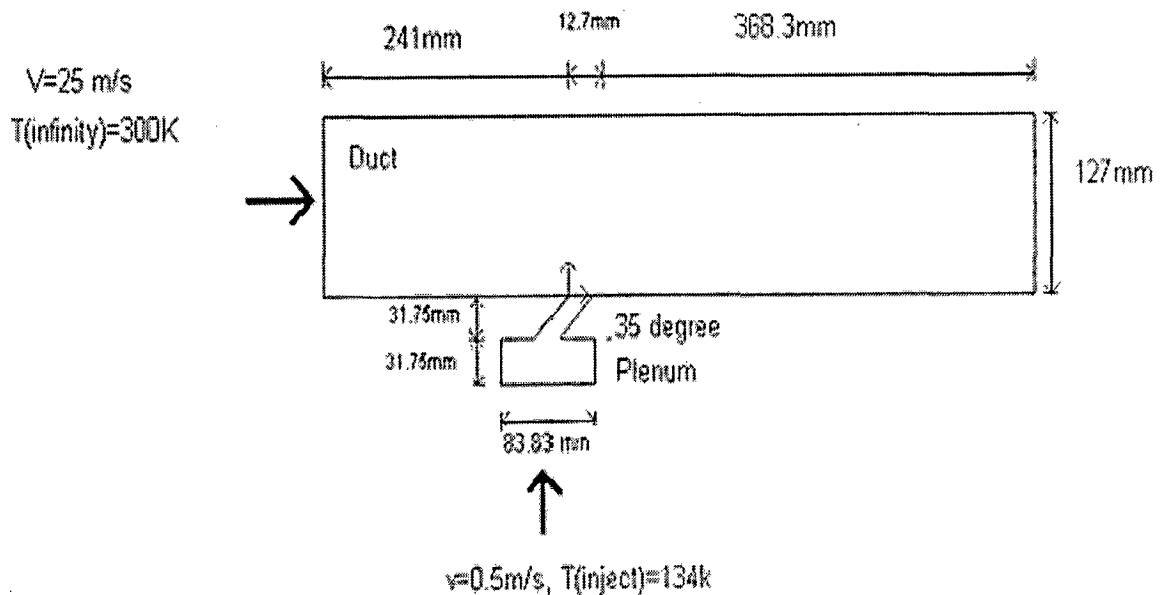


Figure 3.1. Schematic of the Problem, Front view

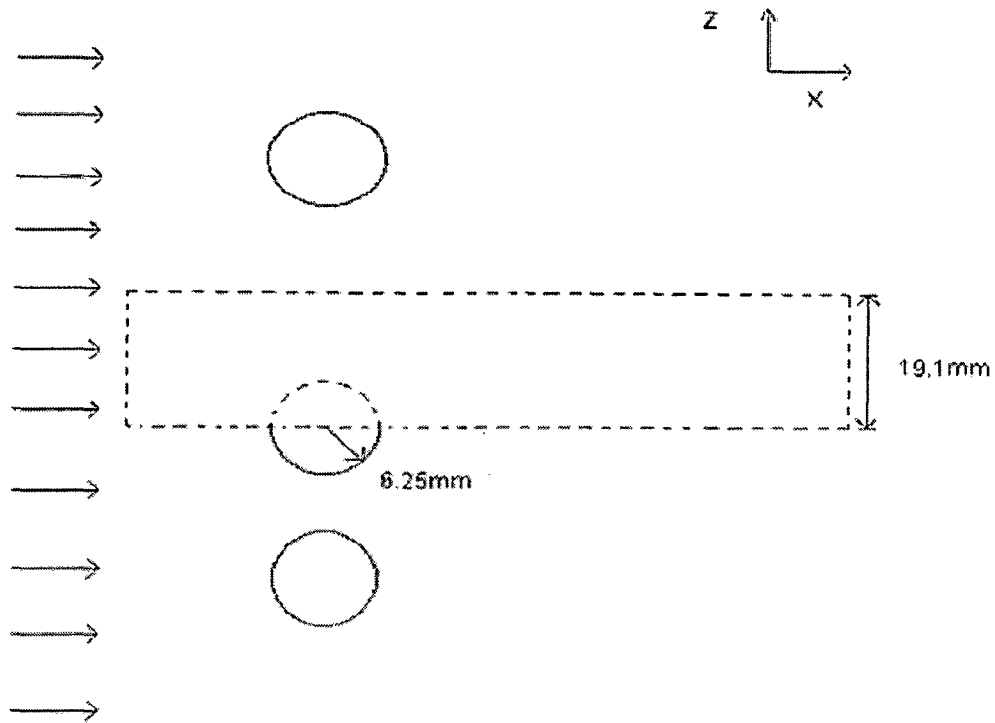


Figure 3.2. Schematic of the Problem, Top View

The bulk temperature of the stream wise air (T_{∞}) is 300K, and the velocity of the air stream is 25 m/s. The bottom wall of the duct that intersects the hole array is assumed to be a completely insulated (adiabatic) wall. The secondary (injected) air enters the plenum at a uniform velocity of 0.5m/s. The temperature of the injected air (T_{inject}) is 134 K. The properties of air $\mu = 0.000017894 \text{ kg/m-s}$ and $C_p = 1006.43 \text{ J/kg-K}$ are used in the model.

3.2 Second Problem Description

3.2.1 NACA2415 Airfoil

Complete specification of NACA-2415 airfoil is given below:

NACA Four-Digit Series: The first digit specifies the maximum camber (m) in percentage of the chord (airfoil length), the second indicates the position of the maximum camber (p) in tenths of chord and the last two numbers provide the maximum thickness (t) of the airfoil in percentage of chord. For example, the NACA-2415 airfoil has a

maximum thickness of 15% with a camber of 2% located 40% back from the airfoil leading edge (or $0.4c$).

3.2.2 Flow field

Consider the flow around a NACA-2415 airfoil at an angle of attack (α) as 10° , 12.5° , 15° and 16° and a free stream Mach number (M_∞) of 0.4066. The chord length C is 1m. Figure 3.3-3.4 depicts the detailed problem with grid generation field.

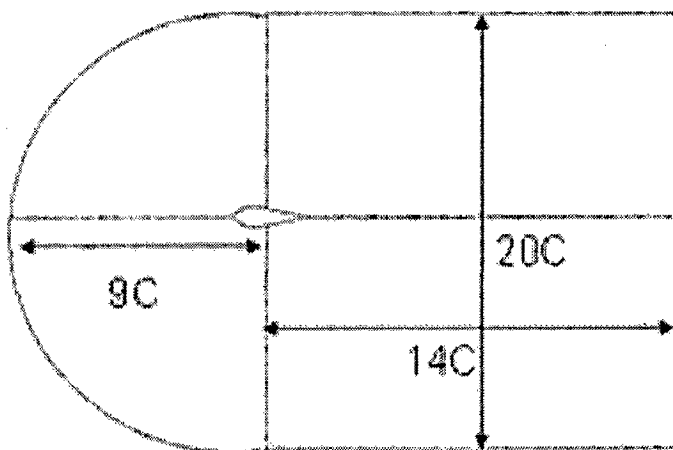


Figure 3.3. Grid generation field

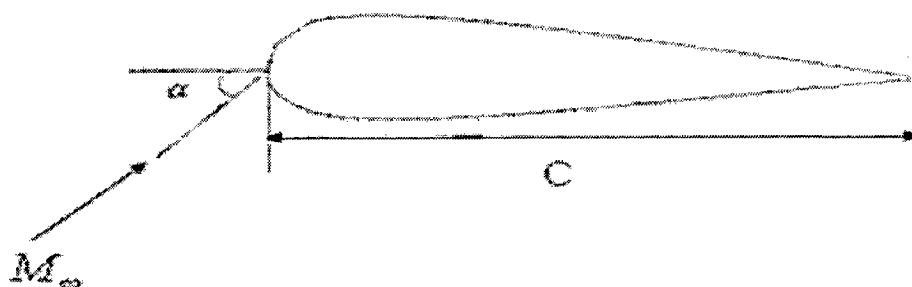


Figure 3.4. Angle of attack (AOA) and chord-length

3.3 Third Problem Description

The dimension of the problem is shown in Figure 3.5.

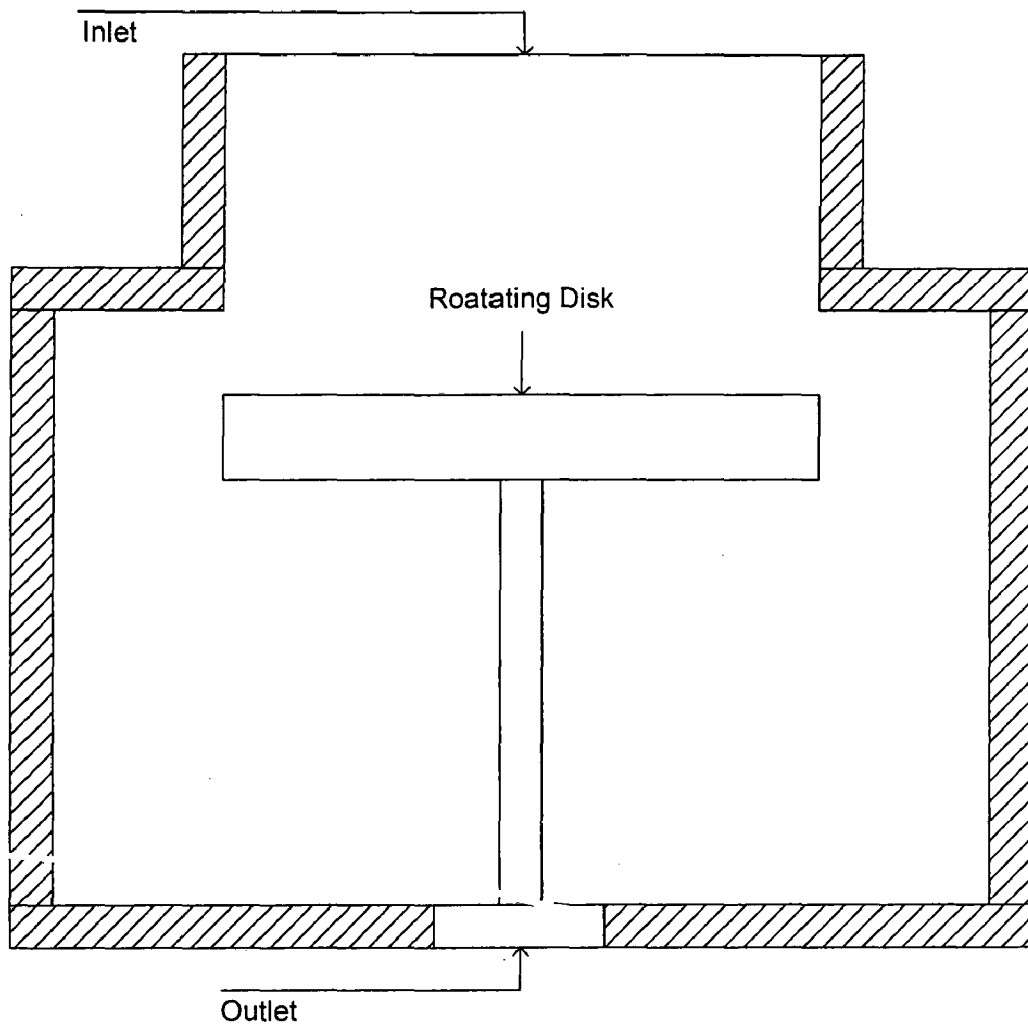
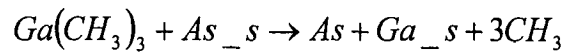


Figure 3.5. Schematic diagram of CVD reactor

A rotating disk CVD reactor for the growth of Gallium Arsenide (GaAs) shown in Figure 3.5 has been modeled. The process gases, Trimethyl Gallium ($\text{Ga}(\text{CH}_3)_3$) and Arsine (AsH_3) enter the reactor at 293 K through the inlet at the top. These gases flow over the hot, spinning disk depositing thin layers of gallium and arsenide on it in a uniform, repeatable manner. The disk rotation generates a radially pumping effect, which forces the gases to flow in a laminar manner down to the growth surface, outward across the disk, and finally to be discharged from the reactor.

The semiconductor materials Ga(s) and As(s) are deposited on the heated surface governed by the following surface reactions.



As mentioned earlier, the inlet gas is a mixture of trimethyl gallium and arsine. In the inlet mixture the mass fraction of $Ga(CH_3)_3$ is 0.15 and AsH_3 is 0.4. The mixture velocity at the inlet is 0.02189 m/s. The disk rotates at 80 rad/sec, and the top wall is heated to 473 K, and the sidewalls of the reactor are maintained at 343 K. The wafer (rotating disk) is heated to a uniform temperature of 1023 K, and the bottom wall is at 303 K. These CVD reactors are typically known as cold-wall reactors, where only the wafer surface is heated to higher temperatures, while the remaining reactor walls are maintained at low temperatures.

MATHEMATICAL MODELING AND METHODOLOGY

4.1 First Problem

4.1.1 Governing Equations

The Navier-Stokes equations for isothermal incompressible flows are written as:

$$\begin{aligned} \frac{\partial u_i}{\partial x_i} &= 0 \\ \frac{\partial u_i}{\partial t} + \frac{\partial u_i u_j}{\partial x_j} &= -\frac{1}{\rho} \frac{\partial p}{\partial x_i} + \nu \frac{\partial^2 u_i}{\partial x_j \partial x_j}, \end{aligned} \quad (4.1)$$

Where u_i the velocity, p is the pressure and ν is the kinematic viscosity. The LES equations are formally derived by applying a filtering operation: a filtered variable is defined as

$$\bar{f}(r, t) = \int_V G(|r - r'|) f(r', t) dr', \quad (4.2)$$

Where V is the volume of filtering and G is the filter function. After filtering Equations (4.1) the LES equations take the following form

$$\begin{aligned} \frac{\partial \bar{u}_i}{\partial x_i} &= 0 \\ \frac{\partial \bar{u}_i}{\partial t} + \frac{\partial \bar{u}_i \bar{u}_j}{\partial x_j} &= -\frac{1}{\rho} \frac{\partial \bar{p}}{\partial x_i} - \frac{\partial \tau_{ij}}{\partial x_j} + \nu \frac{\partial^2 \bar{u}_i}{\partial x_j \partial x_j}, \end{aligned} \quad (4.3)$$

where the SGS stresses are

$$\tau_{ij} = \overline{u_i u_j} - \bar{u}_i \bar{u}_j \quad (4.4)$$

Boussinesq approximation is as follows:

$$\tau_{ij} - \frac{\delta_{ij}}{3} \tau_{kk} = -2\nu_T \bar{S}_{ij} = -\nu_T \left(\frac{\partial \bar{u}_i}{\partial x_j} + \frac{\partial \bar{u}_j}{\partial x_i} \right) \quad (4.5)$$

It relates sub-grid-scale stresses τ_{ij} to the eddy viscosity ν_T the resolved-scale strain rate tensor \bar{S}_{ij} .

The Smagorinsky model for eddy viscosity is written as

$$\nu_T = (C_s \Delta)^2 |\bar{S}|, \quad (4.6)$$

Where C_s is called a Smagorinsky (1963) constant, Δ is a length scale and $|\bar{S}| = \sqrt{2\bar{S}_{ij}\bar{S}_{ij}}$.

The length scale represents the cell size and it is usually computed as $V^{1/3}$. A value 0.18 for C_s has been evaluated for the inertial range dynamics, Lesieur (1997). In the presence of shear flow a smaller value must be used, which was first discovered by Deardorff (1970). He studied a channel flow and found that a smaller value for $C_s=0.1$ had to be used in the presence of a strong shear-driven turbulence. This observation has since been confirmed by many studies. Furthermore, in the vicinity of the walls, the eddy viscosity must be reduced. This is usually carried out with the van Driest damping function. Germano et al (1991) presented a dynamic SGS model, where the model coefficient is calculated during the simulation. This is based on the application of two different filters. In addition to the grid filter G , a test filter \hat{G} is applied. The test filter width $\hat{\Delta}$ is larger than the grid filter width Δ , usually $\hat{\Delta}=2\Delta$. The term grid filter implies that usually discretization takes care of the filtering in numerical computations without any explicit procedure. The grid filter and the test filter are applied to the momentum equations (4.1) to obtain the following equation:

$$\frac{\partial \hat{u}_i}{\partial t} + \frac{\partial \hat{u}}{\partial x_j} = -\frac{1}{\rho} \frac{\partial \hat{p}}{\partial x_i} - \frac{\partial T_{ij}}{\partial x_i} + \nu \frac{\partial^2 \hat{u}_i}{\partial x_j \partial x_j}, \quad (4.7)$$

Where subtest stresses are given by

$$T_{ij} = \overline{u_i u_j} - \hat{u}_i \cdot \hat{u}_j \quad (4.8)$$

The test filter is now applied to the grid-filtered equations (4.3);

$$\frac{\partial \hat{u}_i}{\partial t} + \frac{\partial \hat{u}_i \hat{u}_j}{\partial x_j} = -\frac{1}{\rho} \frac{\partial \hat{p}}{\partial x_i} - \frac{\partial \hat{\tau}_{ij}}{\partial x_i} - \frac{\partial \zeta_{ij}}{\partial x_i} + \nu \frac{\partial^2 \hat{u}_i}{\partial x_j \partial x_j}, \quad (4.9)$$

$$\zeta_{ij} = \overline{u_i u_j} - \hat{u}_i \hat{u}_j \quad (4.10)$$

Using equation (4.7) and (4.9), the expression for ζ_{ij} can be written as

$$\zeta_{ij} = T_{ij} - \hat{\tau}_{ij} \quad (4.11)$$

Equation (4.8) represent the subtest-scale stresses whose length scale is less than the subtest filter width $\hat{\Delta}$, Equation (4.11) represent then the resolved turbulent stresses by the scales between the grid filter width Δ and the subtest filter width $\hat{\Delta}$. Let us model both τ_{ij} and T_{ij} by the same functional form of the Smagorinsky (1963) model:

$$\tau_{ij} - \frac{\delta_{ij}}{3}\tau_{kk} = -2C\Delta^2|\bar{S}|\bar{S}_{ij} = -2C\beta_{ij} \quad (4.12)$$

$$T_{ij} - \frac{\delta_{ij}}{3}T_{kk} = -2C\hat{\Delta}^2|\hat{S}|\hat{S}_{ij} = -2C\alpha_{ij} \quad (4.13)$$

In order to solve 'C' from Equations 4.12 and 4.13 Piomelli and Liu (1995) developed the following localized dynamic model:

$$\zeta_{ij} - \frac{\delta_{ij}}{3}\zeta_{kk} = -2C\alpha_{ij} + 2C\beta_{ij} \quad (4.14)$$

where the coefficient C under the filter is replaced with an estimate C^* , which is assumed to be known. Equation (4.14) can be solved by the contraction:

$$C = -\frac{1}{2} \frac{(\zeta_{ij} - 2C^*\beta)\alpha_{ij}}{\alpha_{mn}\alpha_{mn}} \quad (4.15)$$

4.1.2 Flow Solver

4.1.2 (A) Conservation Form

The continuity equation in a conservation form becomes

$$\int_V \rho V \cdot dS = 0, \quad (4.16)$$

Where ρ is the density and $V = ui^i + vj^j + wk^k$ is the velocity of the fluid. The integration is taken over the control volume faces. This constraint simply states that at every moment the mass flow out from the control volume equals the mass flow in. The momentum equation in the x-direction is written as:

$$\frac{\partial}{\partial t} \int_V \rho u dV + \int_V \rho u V \cdot ndS + \int_V pn_x dS - \int_V \rho g_x dV - \mu \int_V \left(n_x \frac{\partial u}{\partial x} + n_y \frac{\partial u}{\partial y} + n_z \frac{\partial u}{\partial z} \right) dS = 0 \quad (4.17)$$

Here, p is the pressure, ρg_x is the body force and $n = n_x \hat{i} + n_y \hat{j} + n_z \hat{k}$ is a unit normal of the control volume face. The equation in the y-and z-directions are obtained by replacing the velocity component u with v and w and the wall-normal component n_x in the pressure term with n_y and n_z respectively.

4.1.2 (B) Momentum Equations

Cartesian equations are solved sequentially. Within each Cartesian direction, a contribution from all curvilinear grid directions is computed. A following time-stepping method is used in solving Equation (4.17), which, after discretization for a node (i, j, k) becomes

$$V_{ijk} \left(\frac{(1 + \gamma)\rho u^{n+1} - (1 + 2\gamma)\rho u^n + \gamma\rho u^{n-1}}{\Delta t} \right)_{ijk} = - \sum_{\phi=1}^{faces} (\hat{F}_{\phi}^{inv} - \hat{F}_{\phi}^{visc})^{n+1} S_{\phi}, \quad (4.18)$$

Where the parameter γ defines a first order accurate implicit Euler method with value 0 and a second-order accurate three-level implicit method (3-LI) with value 0.5. The inviscid flux in the x-direction at the cell face ϕ is

$$F_{\phi}^{inv} = \hat{F}_{\phi}^{inv} S_{\phi} = S_{\phi} \rho u_{\phi} \hat{V}_{\phi} \cdot \hat{n}_{\phi} + (S n_x p)_{\phi} = n_{\phi} \rho u_{\phi} + (S n_x p)_{\phi}. \quad (4.19)$$

In linearization of the viscous fluxes, a thin-shear-layer approximation is used in each coordinate direction instead of calculating the derivatives by using the generalized divergence theorem of Gauss. This approximation is done to avoid a large molecule in the matrix. In a Cartesian grid, both approximations are the same. At the face $\left(i + \frac{1}{2}, j, k\right)$ (i.e., in the i-direction), the simplified viscous flux for the u-momentum equation becomes

$$F_{i+(1/2),j,k}^{visc} = \frac{S\mu}{\Delta\xi} (u_{i+1,jk} - u_{ijk}) \quad (4.20)$$

Where $\Delta\xi$ is the distance between the nodes (i, j, k) and $(i+1, j, k)$. After linearization, a Poisson type equation is obtained for the velocity increment Δu

$$\sum_{nb} A_{nb} \Delta u_{nb} = - \sum_{\phi=1}^{faces} (S n_x)_{\phi} \Delta p_{\phi} - \sum_{\phi=1}^{faces} (\hat{F}_{\phi}^{inv} - \hat{F}_{\phi}^{visc})^k - D_{ijk}^k, \quad (4.21)$$

where the sum on the left-hand side is over the neighbor nodes. In $\Delta u = u_{ijk}^{n+1} - u_{ijk}^k$ the state k lies between the solved state n and the state n+1 to be computed. The first term on the right hand side includes the pressure at the time level n+1 and in an iterative solution the term is ignored.

Term D_{ijk}^k includes the time derivative as a source term.

4.1.1 (C) Pressure Coupling

The solution of the momentum equation must be coupled with pressure. The last two terms of Equation (4.21) cancel and when the iteration is converged. The linearized increments Δu and Δp are replaced in the following by iterative correction u' and p' :

$$\sum_{nb} A_{nb} u'_{nb} = - \sum_{\phi=1}^{faces} S_{\phi} n_{\phi x} p'_{\phi}, \quad (4.22)$$

where the standard simplification utilized in a SIMPLE method is to drop the non-diagonal terms from Equation (4.22) to derive a manageable equation. The continuity equation states that

$$\sum_{\phi=1}^{facesij} (\rho (V^* + V') \cdot S)_{\phi} = 0 \quad (4.23)$$

$$\sum_{\phi=1}^{facesij} (u' n_x S)_{\phi} + (v' n_y S)_{\phi} + (w' n_z S)_{\phi} = - \sum_{\phi=1}^{facesij} (\rho V^* \cdot S)_{\phi},$$

where V^* is the velocity field that does not obey the mass balance and V' is the iterative correction.

After some assumptions and manipulations of the terms we finally obtain the Poisson equation for the pressure corrections

$$\begin{aligned}
& B_{P,ijk} P'_{ijk} + B_{W,ijk} P'_{i-1,jk} + B_{E,ijk} P'_{i+1,jk} + B_{S,ijk} P'_{i,j-1,k} + B_{N,ijk} P'_{i,j+1,k} + \\
& B_{B,ijk} P'_{ijk-1} + B_{T,ijk} P'_{ijk+1} = -\Delta \tau_{ijk},
\end{aligned} \tag{4.24}$$

where the coefficient can be found in Majander (2000).

4.2 Second Problem

4.2.1 Transport Equation for the Spalart-Allmaras Model

The Spalart-Allmaras model is a simple one-equation model that solves a modeled transport equation for the kinematic eddy (turbulent) viscosity, Spalart and Allmaras (1992). The Spalart-Allmaras model was designed for aerospace applications involving wall bounded flows and has shown to give good results for boundary layers subjected to adverse pressure gradients. In this problem compressible flow exists, therefore, Spalart-Allmaras model is best suited. The transported variable in the Spalart-Allmaras model $\tilde{\nu}$ is identical to the turbulent kinematic viscosity except in the near-wall (viscous-affected) region. The transport equation for $\tilde{\nu}$ is

$$\rho \frac{D\tilde{\nu}}{Dt} = G_\nu + \frac{1}{\sigma_{\tilde{\nu}}} \left[\frac{\partial}{\partial x_j} \left\{ (\mu + \rho \tilde{\nu}) \frac{\partial \tilde{\nu}}{\partial x_j} \right\} + C_{b2} \rho \left(\frac{\partial \tilde{\nu}}{\partial x_j} \right)^2 \right] - Y_\nu \tag{4.25}$$

Where G_ν is the production of turbulent viscosity and Y_ν is the destruction of turbulent viscosity that occurs in the near-wall region due to wall blocking and viscous damping. $\sigma_{\tilde{\nu}}$ and C_{b2} are constants and ν is the molecular kinematic viscosity.

4.2.2 Modeling of the Turbulent Viscosity

$$\text{The turbulent viscosity } \mu_t, \text{ is computed from } \mu_t = \rho \tilde{\nu} f_{\nu 1} \tag{4.26}$$

where the viscous damping function $f_{\nu 1}$ is given by,

$$f_{\nu 1} = \frac{\chi^3}{\chi^3 + C_{\nu 1}^3} \text{ and } \chi = \frac{\tilde{\nu}}{\nu} \tag{4.27}$$

4.2.3 Modeling of the Turbulent Production

The production term G_v , is modeled as

$$G_v = C_{b1} \rho \tilde{S} \tilde{v} \quad (4.28)$$

$$\text{Where, } \tilde{S} = S + \frac{\tilde{v}}{k^2 d^2} f_{v2} \text{ and } f_{v2} = 1 - \frac{\chi}{1 + \chi f_{v1}} \quad (4.29)$$

C_{b1} and k are constants, d is the distance from the wall, and S is a scalar measure of the deformation tensor. As in the original model proposed by Spalart and Allmaras, S is based on the magnitude of the vorticity:

$$S = \sqrt{2\Omega_{ij}\Omega_{ij}} \quad (4.30)$$

Where Ω_{ij} is the mean rate-of-rotation tensor and is defined by

$$\Omega_{ij} = \frac{1}{2} \left(\frac{\partial u_j}{\partial x_i} - \frac{\partial u_i}{\partial x_j} \right) \quad (4.31)$$

Default expression for S has been considered since turbulence is found only where vorticity is generated near walls. However, the effect of mean strain on the turbulence production and a modification to the model have been proposed and incorporated into FLUENT. This modification combines measures of both rotation and strain tensors in the definition of S :

$$S = |\Omega_{ij}| + C_{prod} \min(0, |S_{ij}| - |\Omega_{ij}|) \quad (4.32)$$

$$\text{Where, } C_{prod} = 2.0, |\Omega_{ij}| = \sqrt{2\Omega_{ij}\Omega_{ij}}, |S_{ij}| = \sqrt{2S_{ij}S_{ij}} \quad (4.33)$$

with the mean strain rate, S_{ij} defined as

$$S_{ij} = \frac{1}{2} \left(\frac{\partial u_j}{\partial x_i} + \frac{\partial u_i}{\partial x_j} \right) \quad (4.34)$$

Including both the rotation and strain tensors reduces the production of eddy viscosity and consequently reduces the eddy viscosity itself in regions where the measure of vorticity exceeds that of strain rate. One is to be taken in vortical flows, i.e., flow near the core of a vortex subjected to a pure rotation where turbulence is known to be suppressed. Including both the rotation and strain tensors more correctly accounts for the effects of rotation on turbulence. The default option (including the rotation tensor only) tends to over predict the production of eddy viscosity and hence over predicts the eddy viscosity itself in certain circumstances.

4.2.4 Modeling of the Turbulent Destruction

The destruction term is modeled as,

$$Y_v = C_{w1} \rho f_w \left(\frac{\tilde{v}}{d} \right)^2 \quad (4.35)$$

$$\text{Where } f_w = \beta \left[\frac{1 + C_{w3}^6}{\beta^6 + C_{w3}^6} \right]^{0.1667}, \beta = r + C_{w2} (r^6 - r), r = \frac{\tilde{v}}{\tilde{S} k^2 d^2} \quad (4.36)$$

C_{w1} , C_{w2} , and C_{w3} are constants, and \tilde{S} is given by Equation 4.29. Note that the modification described above to include the effects of mean strain on S will also affect the value of \tilde{S} used to compute r .

The model constants C_{b1} , C_{b2} , $\sigma_{\tilde{v}}$, C_{v1} , C_{w1} , C_{w2} , C_{w3} and k have the following values.

$$C_{b1} = 0.1335, \quad C_{b2} = 0.622, \quad \sigma_{\tilde{v}} = 0.667, \quad C_{v1} = 7.1 \quad C_{w1} = \frac{C_{b1}}{k^2} + \frac{(1 + C_{b2})}{\sigma_{\tilde{v}}}, \quad C_{w2} = 0.3,$$

$$C_{w3} = 2.0, \quad k = 0.41$$

4.3 Solution method adopted in FLUENT 6.2

In the present work working material was air. The high speed compressible flow occurs; consequently all physical properties will depend on the temperature. But, for the sake of

simplicity, we made only two parameters i.e., viscosity and density as temperature dependent and thermal-conductivity and specific heat constants as constant.

Viscosity is a function of temperature. In this problem, Sutherland's viscosity law has been used for determining the viscosity at different temperature. Three coefficient formulas have been employed for accurate value of viscosity. The formula is given below:

$$\mu = \mu_0 \left(\frac{T}{T_0} \right)^{3/2} \frac{T_0 + S}{T + S} \quad (4.37)$$

Sutherland's viscosity law resulted from a kinetic theory by Sutherland (1893) using an idealized intermolecular-force potential.

Where μ is the viscosity in kg/m-s, T is the static temperature in K, μ_0 is a reference value in kg/m-s, T_0 is a reference temperature in K, and S is an effective temperature in K, called the Sutherland constant, which is characteristic of the gas. For air at moderate temperatures and pressures, $\mu_0 = 1.7894 \times 10^{-5}$ kg/m-s, $T_0 = 273.11$ K, and $S = 110.56$ K.

Operating pressure was set at zero to minimize the errors due to pressure fluctuation.

4.3.1 Boundary Conditions

Hence, setting the boundary condition for pressure-far-field (far-field)

The flow Reynolds number is greater than, 1×10^5 .

The velocity can be calculated using the expression $Re = \left[\frac{UH\rho}{\mu} \right]$ (4.38)

Here, $U = 141$ m/s, $H = 1$ m, $\rho = 1.176674$ kg/m³ and $\mu = 1.7894 \times 10^{-5}$ kg/m-s

Then, $Re = 92.8 \times 10^5$.

For four different angle of attack boundary conditions are given in Table 4.1.

Table 4.1. Far-field boundary condition

Angle of Attack	Gauge Pressure (Pascal)	Mach Number	X-component of flow direction (m/s)	Y-component of flow direction (m/s)	Turbulent Viscosity Ratio
10 ⁰	101325	0.4066	0.984807	0.173648	10
12.5 ⁰	101325	0.4066	0.976296	0.21644	10
15 ⁰	101325	0.4066	0.965926,	0.258819	10
16 ⁰	101325	0.4066	0.9612617	0.275637	10

4.3.2 Solution initialization

For airfoil simulations, initialize the flow field using the pressure-far-field boundary as it helps in faster convergence.

The solution initialization at various angles of attack is given in Table 4.2:

Table 4.2. Solution initialization from Far-Field

Angle of Attack	Gauge Pressure (Pascal)	X-velocity (m/s)	Y-velocity (m/s)	Modified Turbulent viscosity (m ² /s)
10 ⁰	101325	138.9817	24.0622	0.0001529736
12.5 ⁰	101325	137.3098	30.5453,	0.0001529736
15 ⁰	101325	136.3171	36.52605	0.0001529736
16 ⁰	101325	135.6589	38.89951	0.0001529736

4.3.3 Solution

Solution for all four AOA, SIMPLE method has been adopted for pressure-velocity coupling, Patankar (1980). For the discretization of density, second order upwind scheme had been used for obtaining coefficient of lift and drag up to 700 iterations, while other parameters, first order upwind scheme had been taken. Second order upwind scheme enables the determination of momentum at higher iteration for 10⁰ AOA and remaining for AOA all equations had been discretized second order upwind scheme.

Lift-coefficient and drag-coefficient had been iterated up to 10000.

After completion lift, drag-coefficient graph, velocity vectors and dynamic pressure contours had been obtained.

4.4 Third problem

The governing equations in non-dimensional form have been implemented for general case. Due to incorporation of chemical reaction with diffusion the complexity of the problem has been increased. The assumption of laminar flow with steady state makes elliptic nature of the governing equations and consequently, takes more computing time and costs. It has been also included the enthalpy transport due to diffusion and thus energy equation will be coupled with the species equations.

Mass balance

$$\frac{\partial(\rho)}{\partial t} + \nabla \cdot (\rho \vec{V}) = 0 \quad (4.39)$$

Momentum Equation

$$\frac{\partial(\rho u_j)}{\partial t} + \nabla \cdot (\rho u_j \vec{V}) = -\frac{\partial p}{\partial x_j} + \nabla \cdot (\mu \nabla u_j) \quad (4.40)$$

Energy Equation

$$\frac{\partial(\rho C_p \theta)}{\partial t} + \nabla \cdot (\rho C_p \theta \vec{V}) + \nabla \cdot \left(\sum h_i \vec{J}_i \right) = -p \nabla \cdot \vec{V} + \nabla \cdot (k \nabla \theta) \quad (4.41)$$

$\vec{V} = u_1 + u_2 + u_3$ $j=1, 2, 3$ in x, y and z directions respectively.

The third term in left hand side of energy equation shows the enthalpy transport due to diffusion.

Species Balance

$$\frac{\partial(\rho Y_i)}{\partial t} + \nabla \cdot (\rho \vec{V} Y_i) = -\nabla \cdot \vec{J}_i + R_i + S_i \quad (4.42)$$

Where R_i is the net rate of production of species i by chemical reaction and S_i is the rate of creation by addition from the dispersed phase and $\vec{J}_i = -\rho D_{i,m} \nabla Y_i$ (4.43)

$D_{i,m}$ is the diffusion co-efficient for species i in the mixture.

Y_i is the mass-fraction of species i in the mixture.

4.4.1 The Laminar Finite-Rate Model

The laminar finite-rate model computes the chemical source terms using Arrhenius expressions and ignores the effects of turbulent fluctuations. The model is exact for laminar flames, but is generally inaccurate for turbulent flames due to highly non-linear Arrhenius chemical kinetics. The laminar model may, however, be acceptable for combustion with relatively slow chemistry and small turbulent fluctuations, such as supersonic flames. The net source of chemical species i due to reaction R_i is computed as the sum of the Arrhenius reaction sources over the NR reactions that the species participate in:

$$R_i = M_{w,i} \sum_{r=1}^{N_R} \hat{R}_{i,r} \quad (4.44)$$

Where, $M_{w,i}$ is the molecular weight of species i and $\hat{R}_{i,r}$ is the Arrhenius molar rate of creation/destruction of species i in reaction r . Reaction may occur in the continuous phase between continuous-phase species only, or at wall surfaces resulting in the surface deposition or evolution of a continuous-phase species.

Consider the r th reaction written in general form as follows:

$$\hat{R}_{i,r} = \Gamma (\nu''_{i,r} - \nu'_{i,r}) \left(K_{f,r} \prod_{j=1}^{N_r} [C_{j,r}]^{\eta'_{j,r}} - K_{b,r} \prod_{j=1}^{N_r} [C_{j,r}]^{\eta''_{j,r}} \right) \quad (4.45)$$

N_r = number of chemical species in reaction r

$C_{j,r}$ = molar concentration of each reactant and product species j in reaction r
(kgmol/m³)

$\eta'_{j,r}$ = forward rate exponent for each reactant and product species j in reaction r

$\eta''_{j,r}$ = backward rate exponent for each reactant and product species j in reaction r

$\nu'_{i,r}$ = stoichiometric coefficient for reactant i in reaction r

$\nu''_{i,r}$ = stoichiometric coefficient for product i in reaction r

$K_{f,r}$ = forward rate constant for reaction r

$K_{b,r}$ = backward rate constant for reaction r

Γ = Net effect of third body on reaction rate

4.4.2 Boundary conditions and material properties

In this problem, the net effect of third body reaction rate has been neglected. The density can be calculated by the ideal gas law. The other fluid properties such as the viscosity μ , thermal conductivity k , specific heat, are evaluated by kinetic theory of gas. The reaction rate constant K' has been changed by Arrhenius' Law as written in equation. K'_0 = pre-exponential factor (PEF), E = Activation energy (AE), m = Temperature exponent (TE), for trimethyl gallium with As (s) reaction, PEF = $1 \times 10^{+06}$, AE = 0 and $m = 0.5$ and for reaction of AsH₃ with Ga (s) these are 10^{+12} , 0 and 0.5 respectively.

The material properties have been set up as shown in Table 4.3 and 4.4.

The discretization method, for Pressure standard method, while for momentum and energy equation and species equations first order upwind scheme have been employed. The correction of pressure and velocity field SIMPLE (Semi-Implicit Method for Pressure Linked Equation) method has been applied.

For AsH₃ following properties has been employed.

Table 4.3. AsH₃ material properties

Parameter	Value
C _p	Kinetic-theory
Thermal Conductivity	Kinetic-theory
Viscosity	Kinetic-theory
Molecular Weight	77.95
Standard State Enthalpy	0
Standard State Entropy	130579.1
Reference Temperature	298.15
L-J Characteristic Length	4.145
L-J Energy Parameter	259.8
Degree of Freedom	0

In this problem, grid has been developed around the flow field in 3D and generated very fine 36645 grids.

Residual of the order 1×10^{-03} for all equations except the energy equation for which it has been taken 1×10^{-06} . The convergence of the problem requires under-relaxation factor and following value has been taken as shown in Table 4.5.

The computations has been performed on IBM PC with 1GB of RAM 2.66GHz Pentium-4 CPU, using CFD commercial code, FLUENT 6.2.

Table 4.4. Material properties for other chemicals

Parameter	Ga(CH ₃) ₃	CH ₃	H ₂	Ga_s	As_s	Ga	As
Name	Tmg	Ch3g	hydrogen	ga_s	as_s	ga	as
Chemical formula	ga<ch3>3	ch3	h2	ga_s	as_s	ga	as
Cp	Kinetic theory	Kinetic theory	Kinetic theory	520.64	520.64	1006.43	1006.43
Thermal-Conductivity	Kinetic theory	Kinetic theory	Kinetic theory	0.0158	0.0158	Kinetic theory	Kinetic theory
Viscosity	Kinetic theory	Kinetic theory	Kinetic theory	2.125e-05	2.125e-05	Kinetic theory	Kinetic theory
Molecular Weight	114.83	15	2.02	69.72	74.92	69.72	74.92
Standard State Enthalpy	0	2.044e+07	0	-3117.71	-3117.71	0	0
Standard State Entropy	130579.1	257367.6	130579.1	154719.3	154719.3	0	0
Reference temperature	298.15	298.15	298.15	298.15	298.15	298.15	298.15
L-J Characteristic length	5.68	3.758	2.827	-	-	0	0
L-J Energy parameter	398	148.6	59.7	-	-	0	0
Degree of Freedom	0	0	5	-	-	-	-

Table 4.5. URF for various parameters

Parameter	URF
Pressure	0.1
Density	0.3
Body Forces	1
Momentum	0.2
ash3	1
ga<ch3>3	1
ch3	1
Energy	0.9

RESULTS AND DISCUSSION

5.1 First Problem

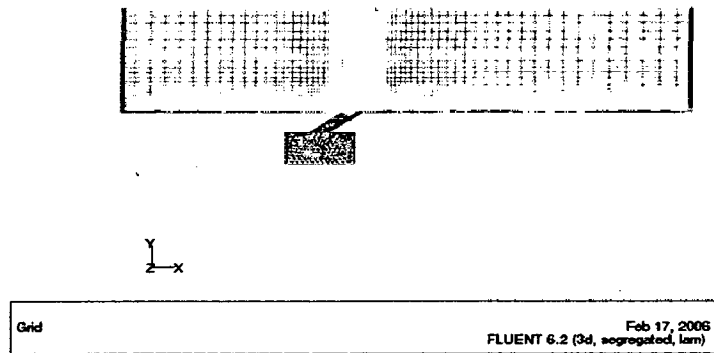


Figure 5.1. Grid generations by FLUENT6.2

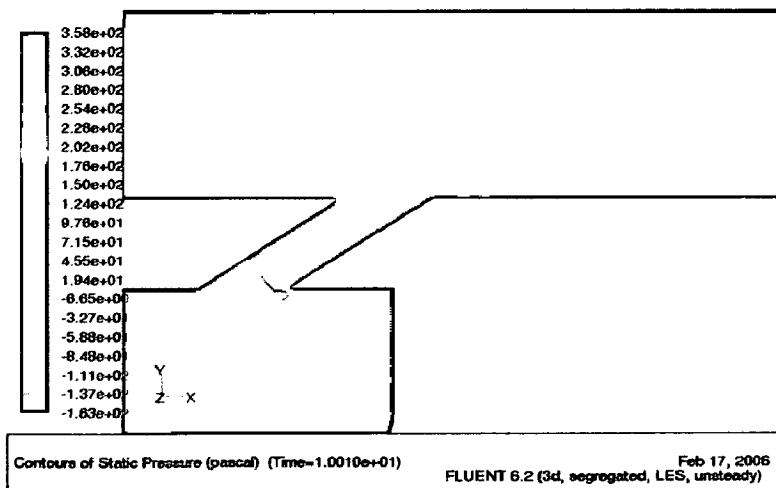


Figure 5.2. Static pressure contour at 10sec

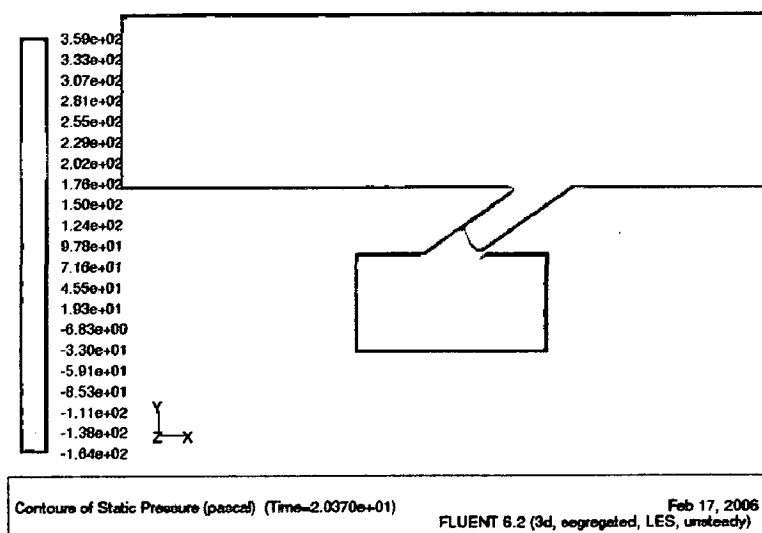


Figure 5.3. Static pressure contour at 20.37sec

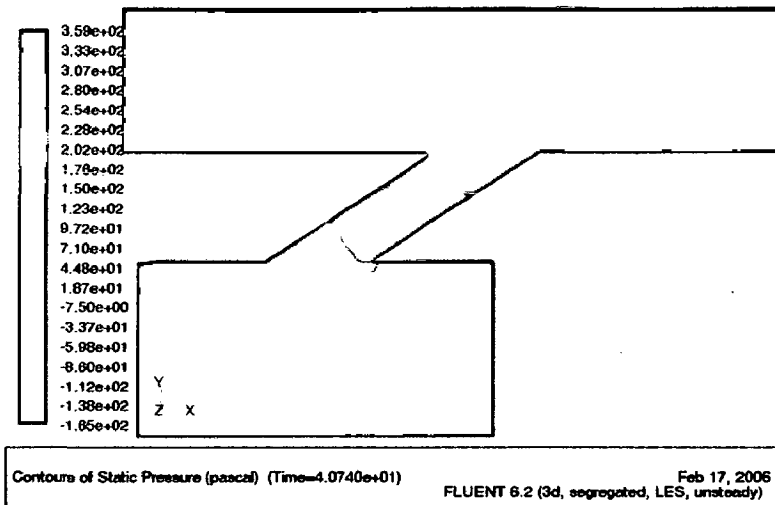


Figure 5.4. Static pressure contours at 40.74sec

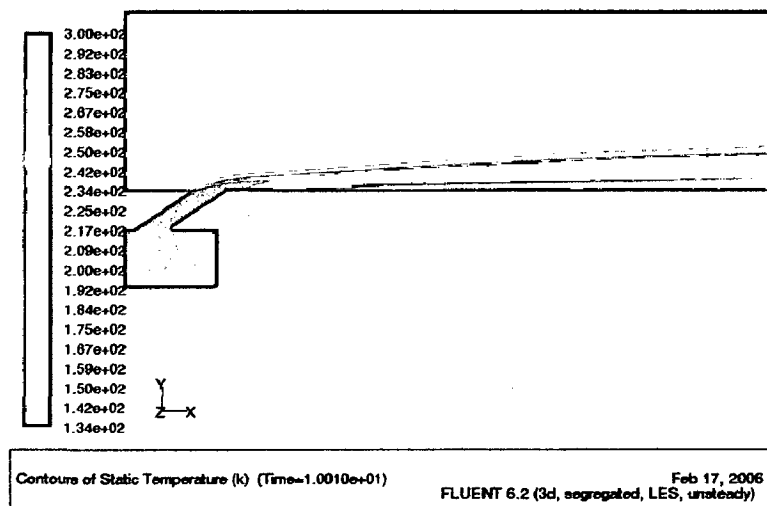


Figure 5.5. Static temperature contours at 10sec

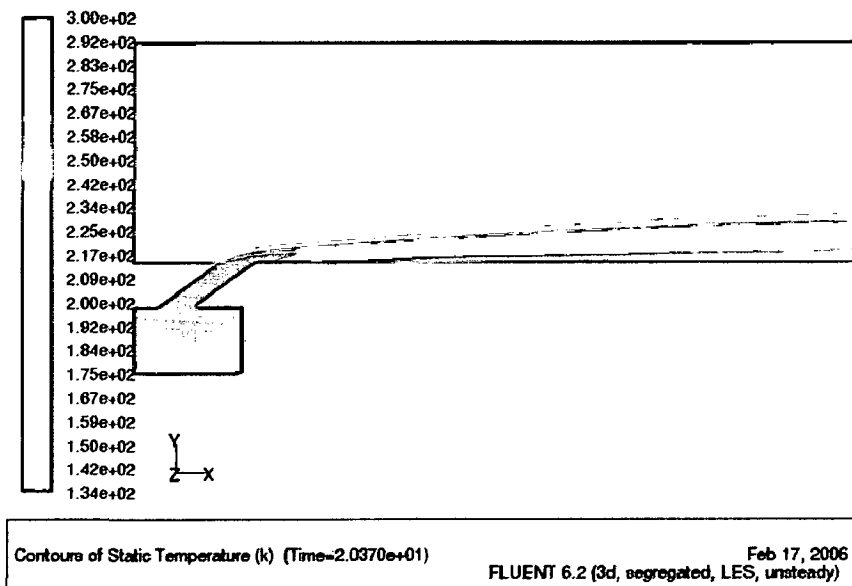


Figure 5.6. Static temperature contours at 20.37sec

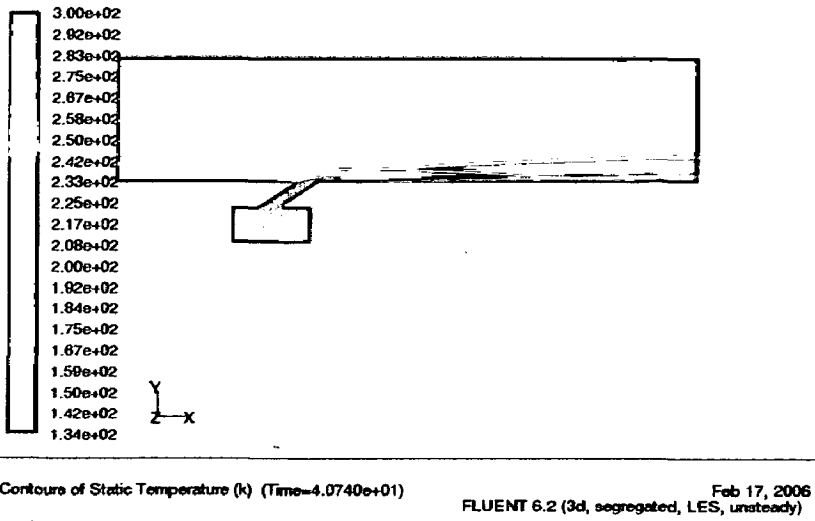


Figure 5.7. Static temperature contours at 40.74sec

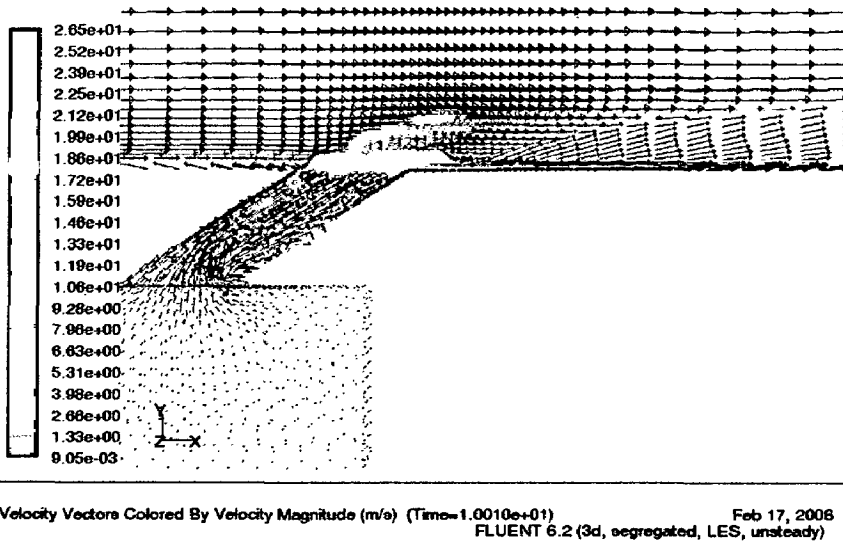


Figure 5.8. Velocity Vectors at 10sec

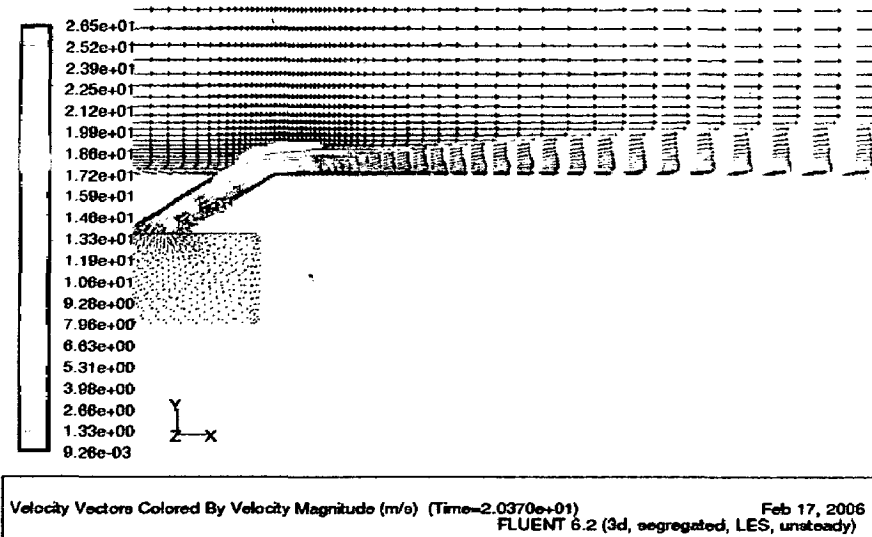


Figure 5.9. Velocity Vectors at 20.37sec

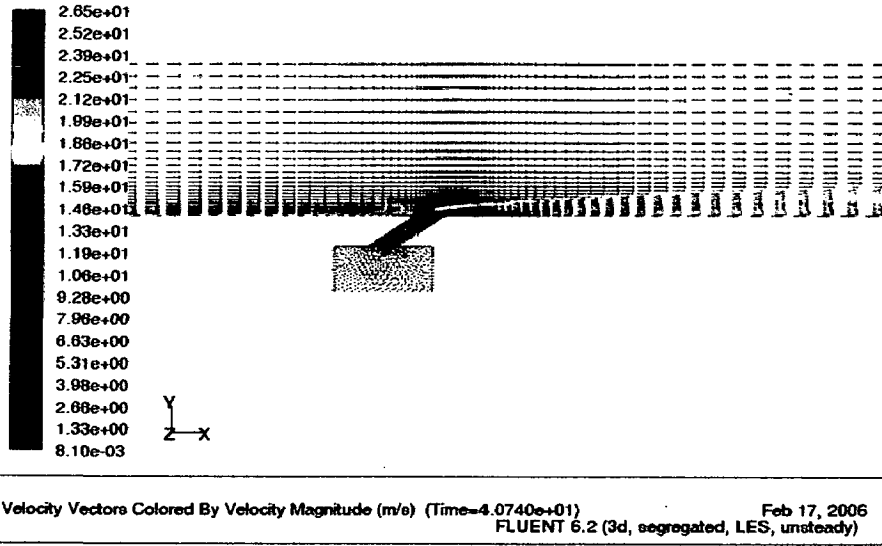


Figure 5.10. Velocity Vectors at 40.74sec

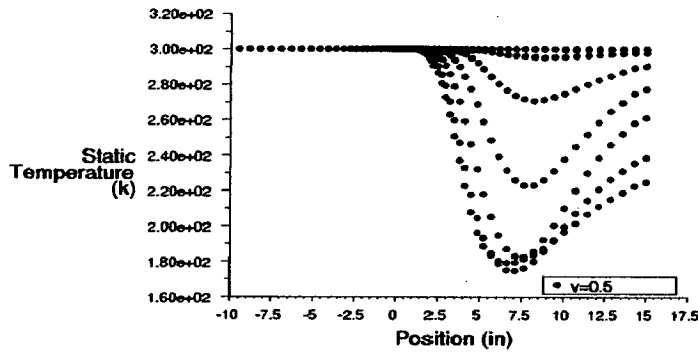


Figure 5.11. Static temperature profile at Iso-surface $y=12.74\text{mm}$ (0.5in) after 20.37sec

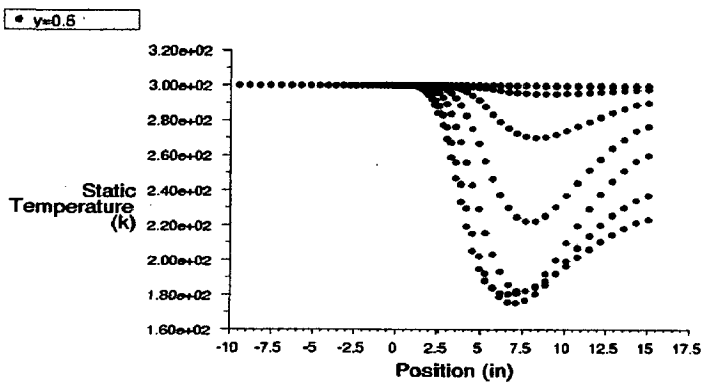


Figure 5.12. Static temperature profile at Iso-surface $y=0.5\text{in}$ after 40.74sec

The grids have been generated in the flow field (Figure 5.1). The pressure contours have been obtained at different time interval (Figure 5.2-5.4) back pressure has been developed at the corner of the duct-plenum interface. It can be minimized by adopting smooth corner at the interface. The minimum and maximum pressure -163 Pascal and 358 Pascal at 10sec and after 20.37sec -164 Pascal to 359 Pascal, while at 40.74sec -165 Pascal to 359 Pascal have been found.

In every time interval, in duct side at left side lower pressure have found than that of right it should maintain at all time interval so that the flow would be maintained.

The Static temperature contours interval -134degreeK to 300degreeK have been registered (Figure 5.5-5.7). The cooling have been started from the axis $y=0$ in the direction where plenum injected the fluid.

The velocity vectors have been obtained at different time interval (Figure 8-10). The maximum velocity has been constant at every time interval i.e., 26.5m/s. while minimum velocity 0.009m/s, 0.0093m/s and 0.0081m/s have been noticed at 10sec, 20.37sec and 40.74sec respectively. In the duct where the temperature is lower velocity is low. The thermal boundary layers have been developed. Here cooling mechanism is convection, after 10sec, in the boundary layer region 15.9m/s velocity has been registered, while after 20.37sec and 40.74sec 17.2m/s and 18.6m/s have been found. Therefore for improving the cooling there should be higher velocity in the duct, the results have found appreciated our aim.

The static temperature profile at 20.37sec and 40.74sec have been obtained (Figure 5.11-5.12) at iso-surface $y=12.74\text{mm}$ (0.5inch). It has been found that at near wall vicinity lower temperature about 180degreeK means cooling have improved as time goes.

Therefore, we can improve the cooling effect by increasing the cooled fluid velocity into the duct, providing the smooth corner for eliminating the back pressure, which hinders the cooling effect. As well as, employing the turbulence into the duct so that cooled fluid could distributed evenly into the duct, would take less time for cooling of turbine duct. In this way, reducing the cooling time, we can prevent the distortion of gas turbine vane, which is exposed to combustion zone.

5.2 Second Problem

Figure 5.13 shows the grid around the airfoil used for simulation. Lift and drag coefficient have been found for various AOA as 10° , 12.5° , 15° and 16° using FLUENT6.2.

Lift-coefficient for 10° (Figure 5.14), 12.5° (Figure 5.15), 15° (Figure 5.16) and 16° (Figure 5.17) AOA have been found 1.115, 1.23, 1.16 and 1.055 respectively. Drag-coefficient for 10° (Figure 5.18), 12.5° (Figure 5.19), 15° (Figure 5.20) and 16° (Figure 5.21) AOA have been found 0.02, 0.03, 0.055 and 0.07 respectively.

At 12.5° angle of attack lift-coefficient is maximum. At 15° angle of attack, drag-coefficient is increased but lift coefficient is reduced, but at 16° the lift has less value while drag is at high value. Velocity vectors and dynamic pressure contours plot were obtained by FLUENT 6.2

Velocity Vectors for 10° (Figure 5.22), 12.5° (Figure 5.23) 15° (Figure 5.24) and 16° (Figure 5.25) have been drawn. According to these figures, the highest velocity is at leading edge of the profile are 427 ms^{-1} for 15° AOA 424 ms^{-1} for 16° AOA. But this highest velocity covers very small area of the top airfoil (Figure 5.25). For 10° AOA, maximum velocity is 319 ms^{-1} but it covers large area of top air profile. For 12.5° AOA, maximum velocity is 393 ms^{-1} and it covers largest area than that of 10° AOA.

Dynamic Pressure contours for 10° (Figure 5.26), 12.5° (Figure 5.27), 15° (Figure 5.28) and 16° (Figure 5.29) AOA shows the maximum dynamic pressure at 16° AOA, but it covers lowest top area of the foil. Consequently, loss of lift-coefficient has noticed and

vortices have been found at the trailing edges of the blade profile at 15° and 16° . But at 16° it is considerable, stalling phenomena predominates and back flow of the mass would occur. It has also been concluded that pressure fluctuation is maximum at 16° angle of incidence. It has also found from velocity vectors and Dynamic pressure contours that stall propagation has been started from 12.5° angle of attack of the flow.

The Figure 5.30 has been obtained by NACA (National Advisory Committee For Aeronautics) for NACA2415 airfoil, they have found the stall angle 12.5° , the FLUENT result shows that 12.5° . The maximum lift at stall angle is 1.27 by experiment but in this analysis 1.23. Then error is about -3.1% which is in acceptable limit.

While the velocity vectors, static pressure and Mach-number contours depicts nearly accurate result

At 12.5° AOA dynamic pressure covers maximum top area of the blade profile. Consequently, the flow efficiency of the blade will enhance when the compressor work at that angle of attack.

Therefore, it can also be suggested that use of NACA2415 airfoil as blade profile causes no any problems. It will perform at maximum efficiency at 12.5° angle of attack.

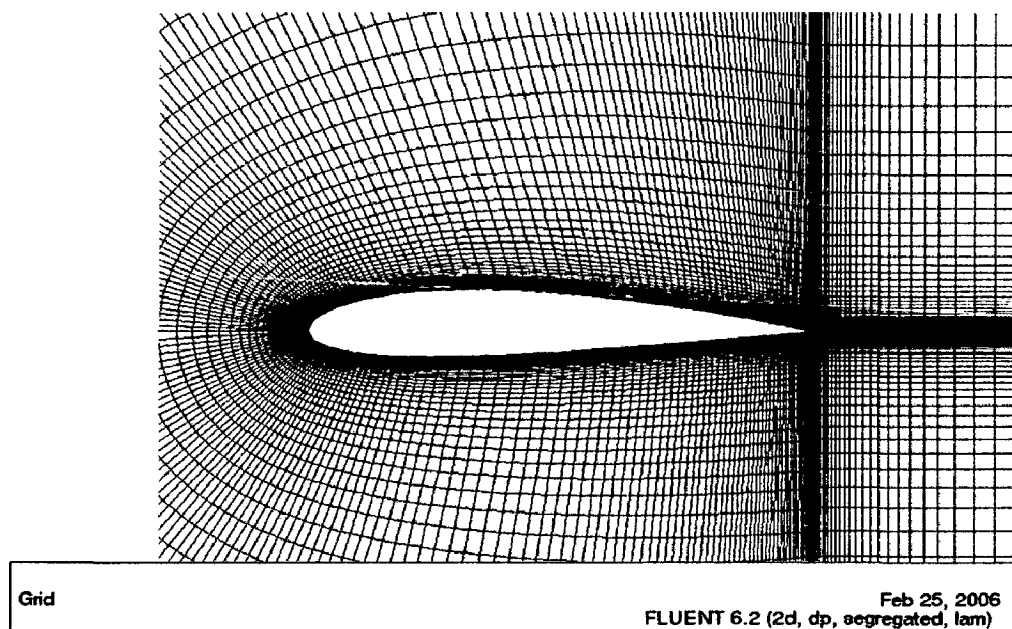
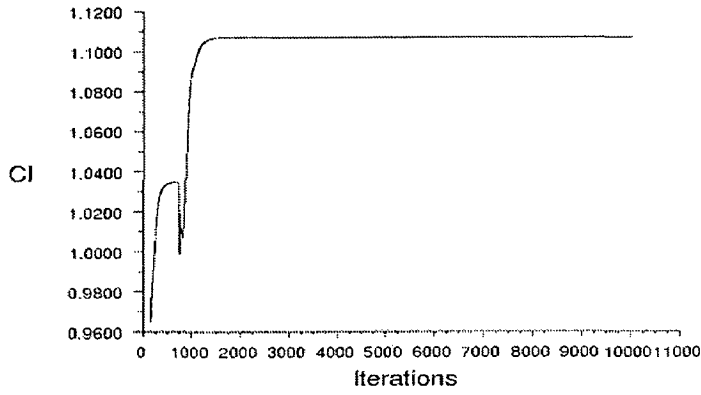
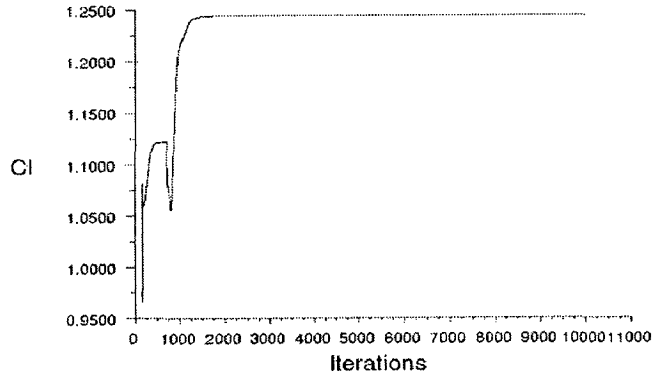


Figure 5.13. Grid generation around airfoil



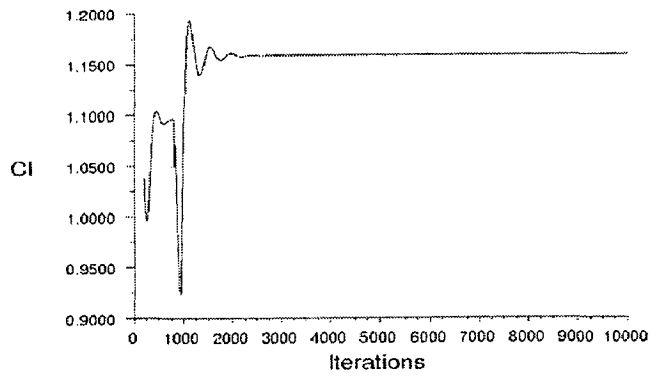
Lift Convergence History Feb 25, 2006
FLUENT 6.2 (2d, dp, segregated, S-A)

Figure 5.14. Lift-coefficient at 10⁰ AOA



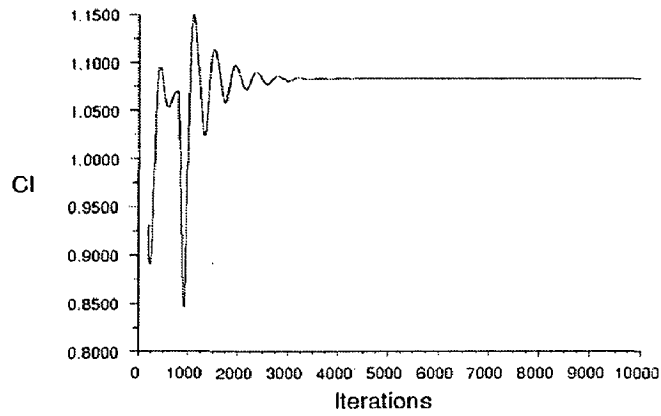
Lift Convergence History Feb 25, 2006
FLUENT 6.2 (2d, dp, segregated, S-A)

Figure 5.15. Lift-coefficient at 12.5⁰ AOA



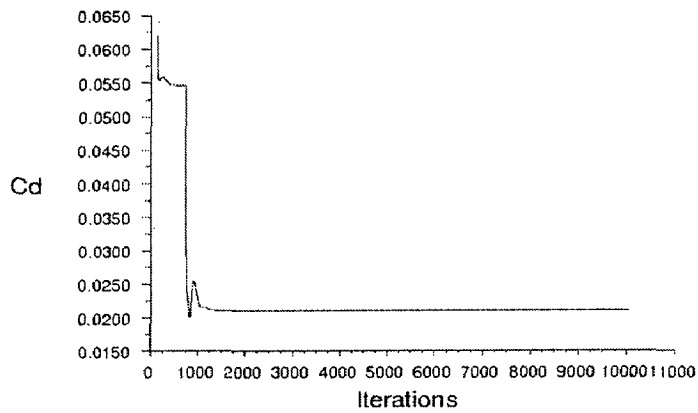
Lift Convergence History Feb 25, 2006
FLUENT 6.2 (2d, dp, segregated, S-A)

Figure 5.16. Lift-coefficient at 15⁰ AOA



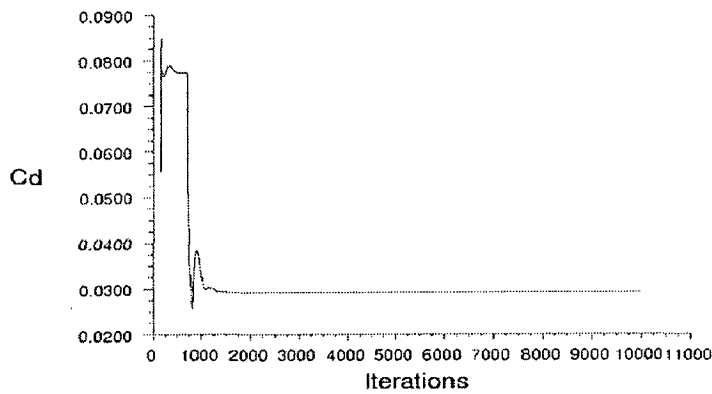
Lift Convergence History Feb 25, 2006
FLUENT 6.2 (2d, dp, segregated, S-A)

Figure 5.17. Lift-coefficient at 16⁰ AOA



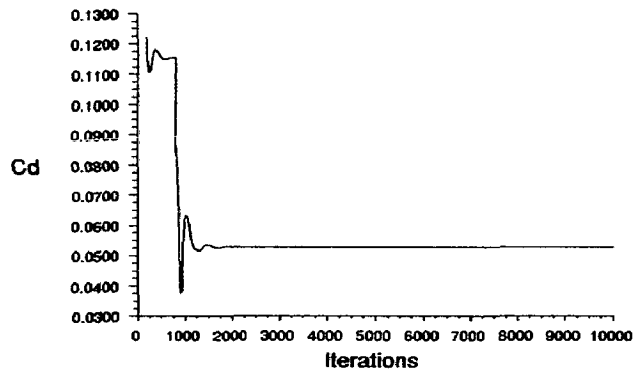
Drag Convergence History Feb 25, 2006
FLUENT 6.2 (2d, dp, segregated, S-A)

Figure 5.18. Drag-coefficient at 10⁰ AOA



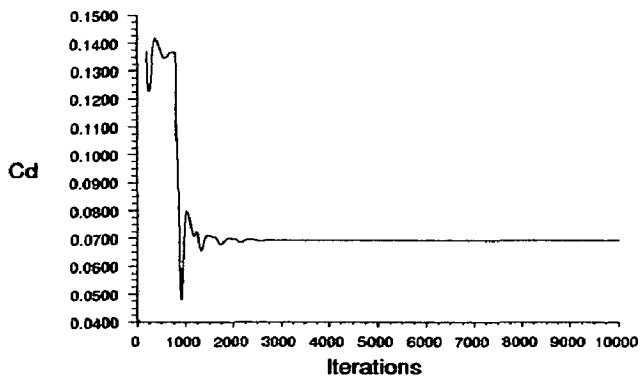
Drag Convergence History Feb 25, 2006
FLUENT 6.2 (2d, dp, segregated, S-A)

Figure 5.19. Drag-coefficient at 12.5⁰ AOA



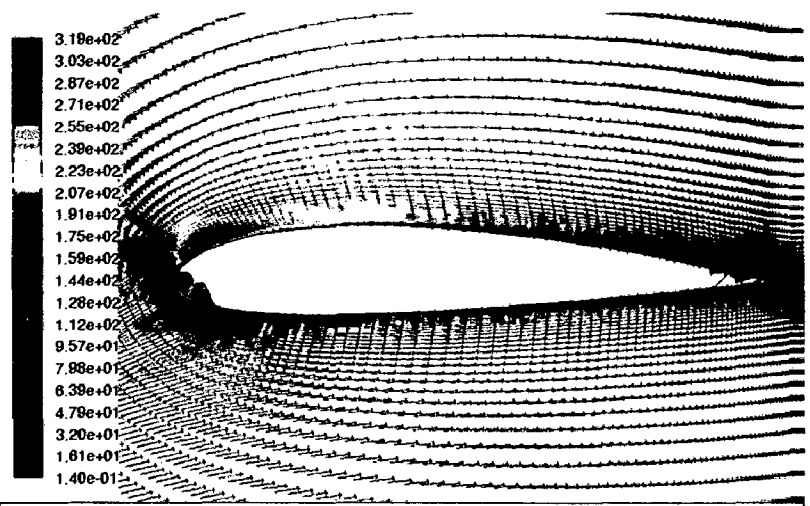
Drag Convergence History Feb 25, 2006
 FLUENT 6.2 (2d, dp, segregated, S-A)

Figure 5.20. Drag-coefficient at 15⁰ AOA



Drag Convergence History Feb 25, 2006
 FLUENT 6.2 (2d, dp, segregated, S-A)

Figure 5.21. Drag-coefficient at 16⁰ AOA



Velocity Vectors Colored By Velocity Magnitude (m/s) Feb 25, 2006
 FLUENT 6.2 (2d, dp, segregated, S-A)

Figure 5.22. Velocity Vectors at 10⁰ AOA

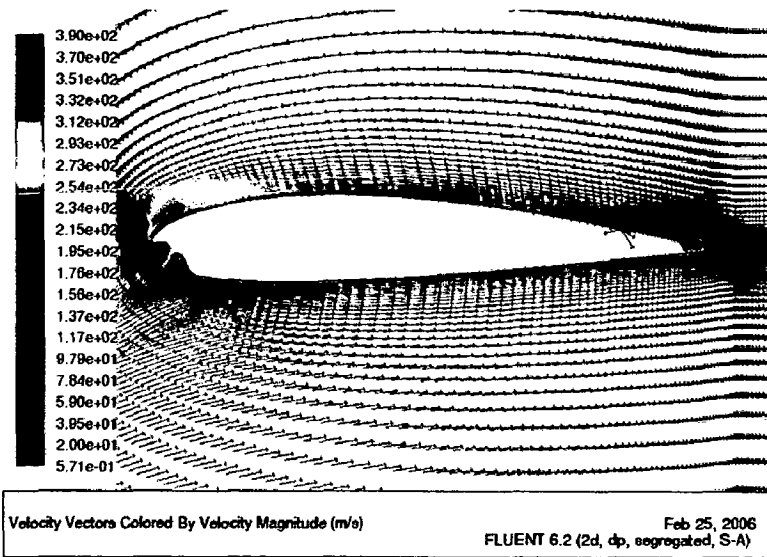


Figure 5.23. Velocity Vectors at 12.5° AOA

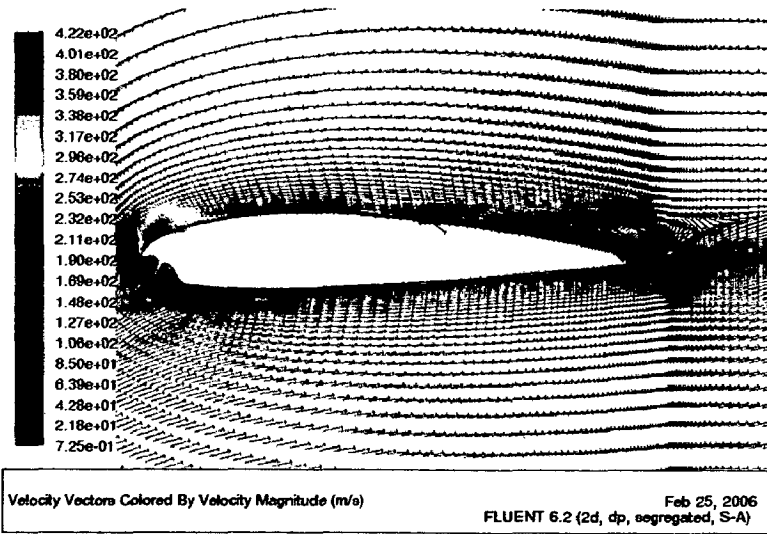


Figure 5.24. Velocity Vectors at 15° AOA

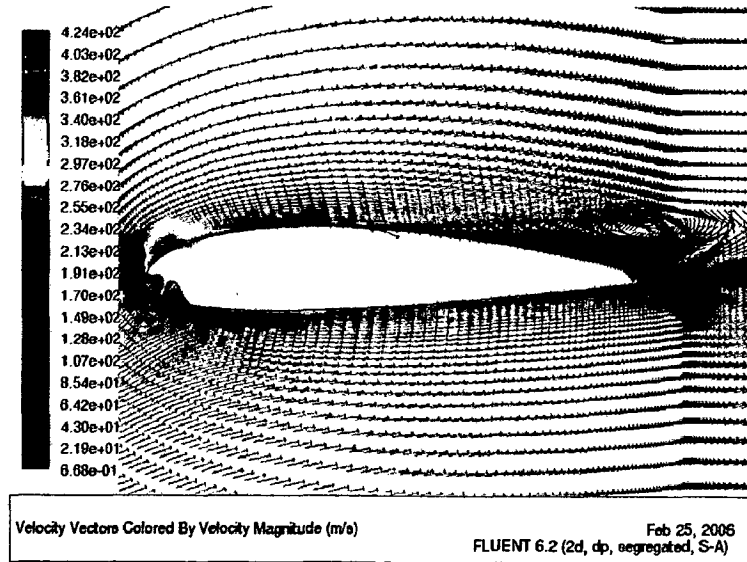


Figure 5.25. Velocity Vectors at 16° AOA

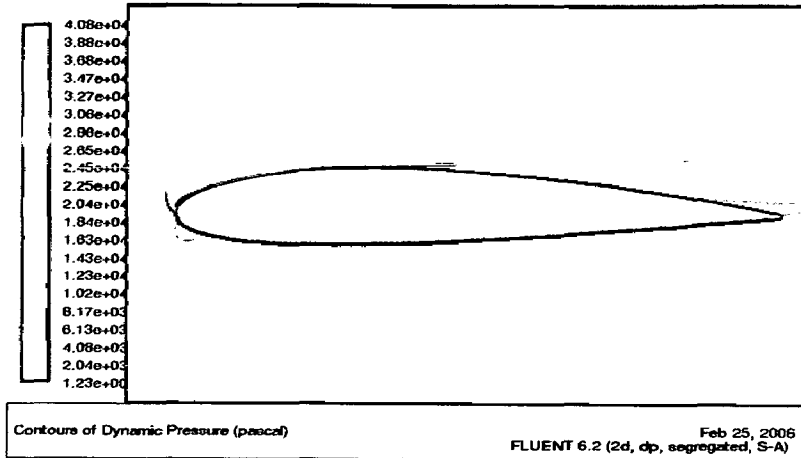


Figure 5.26. pressure contours at 10° AOA

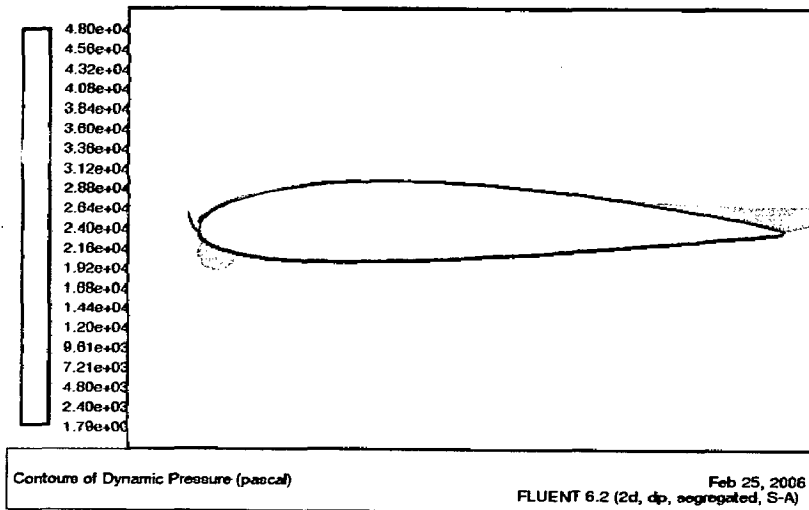


Figure 5.27. pressure contours at 12.5° AOA

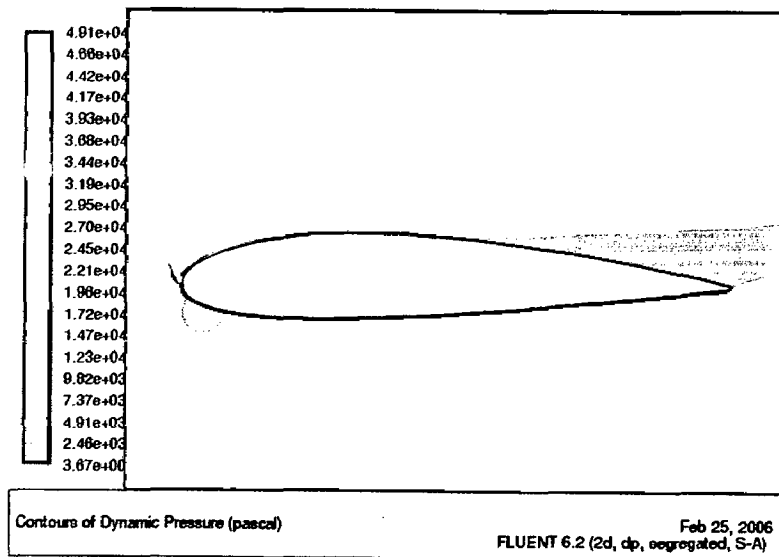


Figure 5.28. pressure contours at 15° AOA

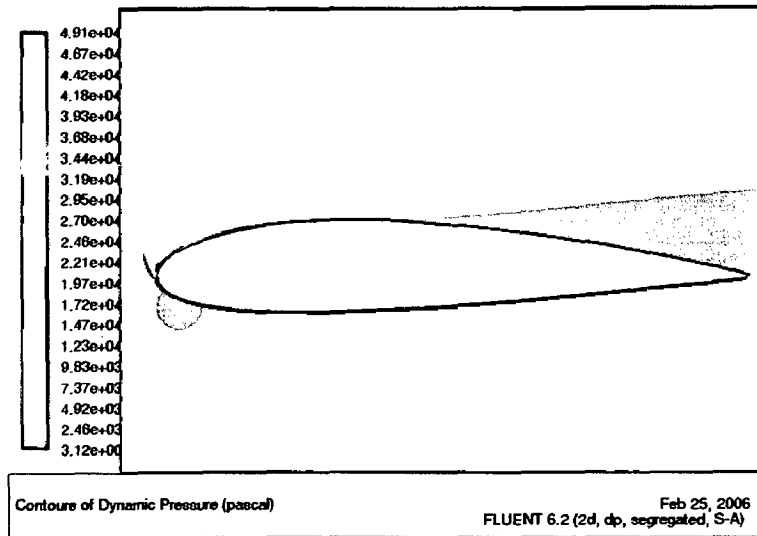


Figure 5.29. Dynamic pressure contours at 16° AOA

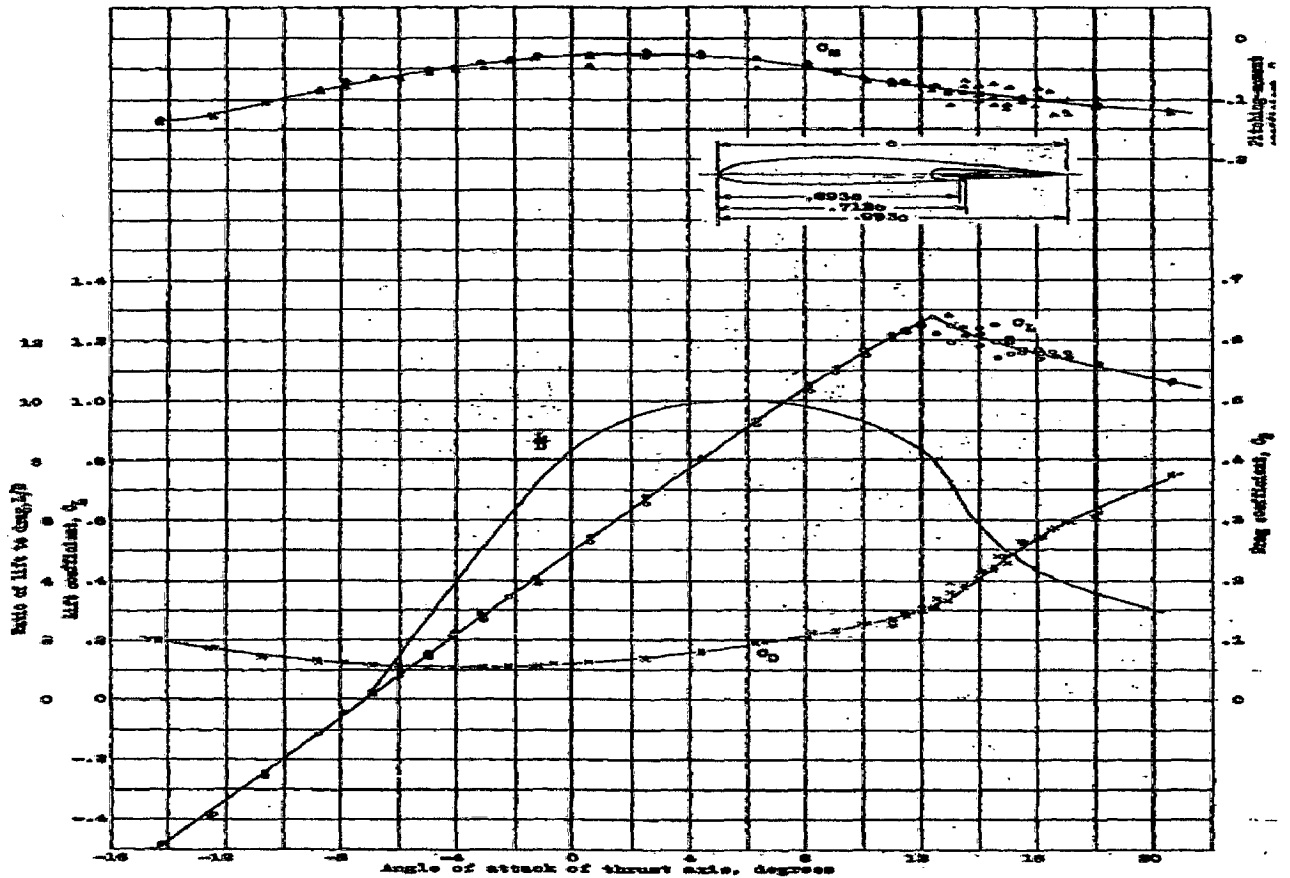


Figure 5a.- Aerodynamic characteristics of Fairchild-22 airplane with 30-percent Fowler flap. Flap retracted. Propeller and horizontal tail surfaces removed. Results corrected for tunnel effects. Test velocity, approximately 50 m.p.h.

Figure 5.30. Stall Angle for NACA-2415 airfoil

Source : Langley Memorial Aeronautical Laboratory, Technical Note No: 578, August 1936, Dearborn and Saule (1936).

5.3 Third Problem

At various rotation speeds the deposition rates of gallium and arsenic have been found. In our problem, the wafer diameter is 0.28m. Due to symmetry of the wafer, the plots of deposition rate have been obtained only for half of the wafer. The inlet velocity of the mixture of chemicals Trimethyl Gallium ($\text{Ga}(\text{CH}_3)_3$) and Arsine (AsH_3) are kept constant. Only rotation speed of wafer has been varied. These have examined at various speeds such as 10rad/s, 20rad/s, 40rad/s, 70rad/s, 110rad/sec and 120rad/s.

At 10rad/sec (Figure 5.31-5.34), $6.99 \times 10^{-5} \text{ kg/m}^2\text{-s}$ for gallium and $7.51 \times 10^{-5} \text{ kg/m}^2\text{-s}$ for arsenic deposition rates on wafer have been found. The contours (Figure 5.31-5.32) and plots (Figure 5.33-5.34) of deposition rate advocate the non-uniformity of deposition of both gallium and arsenic. The plot of deposition gives the picture of polynomial decrement of the rate from center of wafer to edge of the wafer.

At 20rad/s (Figure 5.35-5.38) $5.04 \times 10^{-5} \text{ kg/m}^2\text{-s}$ for gallium and $5.42 \times 10^{-5} \text{ kg/m}^2\text{-s}$ for arsenic deposition rates on wafer have been found. The non-uniformity of deposition exists. The contours (Figure 5.35-5.36) and plots (Figure 5.37-5.38) tells that from center of the wafer to 0.025m radius of the wafer the deposition rate increases after that it decreases but not in polynomial manner. But, still aberration from straight line has been seen.

At 40rad/s (Figure 5.39-5.42) $4.37 \times 10^{-5} \text{ kg/m}^2\text{-s}$ for gallium and $4.70 \times 10^{-5} \text{ kg/m}^2\text{-s}$ for arsenic deposition rates on wafer have been found. The contours of gallium (Figure 5.39) and arsenic (Figure 5.40)

There lower rate of deposition around the center has been found. The plots of deposition rate along the wafer line (Figure 5.41-5.42) it has been found that from center to 0.03m radius of the wafer non-uniform deposition of gallium and arsenic have been found. After 0.03m radius of the wafer still deviation from straight line has been found.

At 70rad/s (Figure 5.43-5.46), $4.40 \times 10^{-5} \text{ kg/m}^2\text{-s}$ for gallium and $4.73 \times 10^{-5} \text{ kg/m}^2\text{-s}$ for arsenic deposition rates on wafer have been found.

The contours of deposition rate (Figure 5.43-5.44) give the picture of non-uniform distributions of gallium and arsenic around the center. The position of the non-uniformity

is around the 0.03m radius of wafer as shown in Figure 5.45-5.46. After this position still, some aberration from the uniform distribution has been found.

At 110rad/s (Figure 5.47-5.50), $4.44 \times 10^{-5} \text{ kg/m}^2 \cdot \text{s}$ for gallium and $4.78 \times 10^{-5} \text{ kg/m}^2 \cdot \text{s}$ for arsenic deposition rates have been found.

The non-uniformity around the center of the wafer has been decreased considerably as shown in the Figure 5.47-5.48. There is very less aberration from the uniform distribution of gallium and arsenic has been registered as shown in Figure 5.49-5.50.

It has been pointed out that deposition rate for 110rad/s and 120rad/s are same.

The uniform distribution of the gallium and arsenic has been found around the center of the wafer as Figure 5.51-5.52 shows. The plot of the deposition rate is also uniform for both gallium and arsenic shown in Figure 5.53-5.54.

We have found near about the uniform distribution of the gallium and arsenic at 120rad/s. Therefore, optimized speed of the wafer is 120rad/s. Where velocity 0.02189m/s and wafer temperature 1023K have been kept constant and radius is 0.14m.

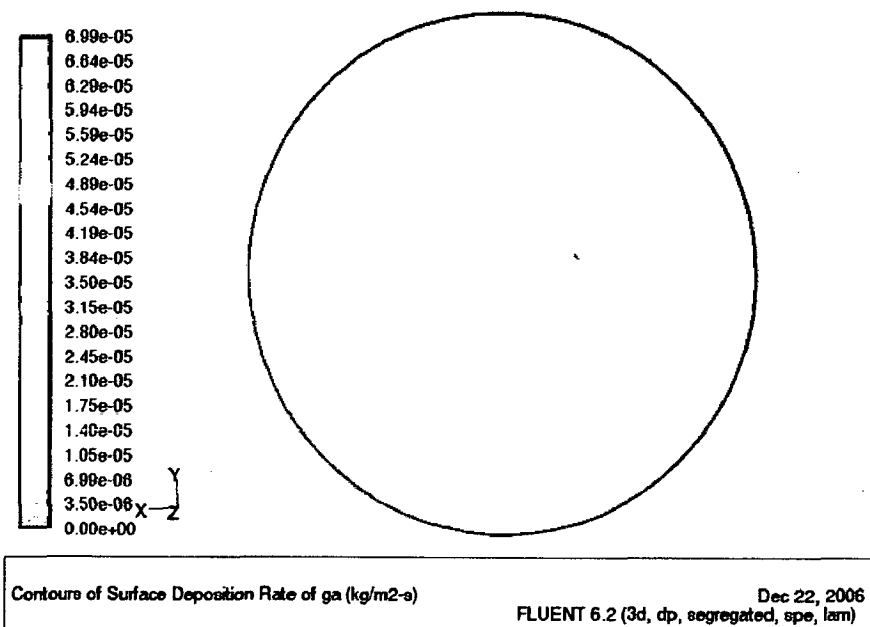


Figure 5.31. Contours of gallium deposition rate 10rad/s

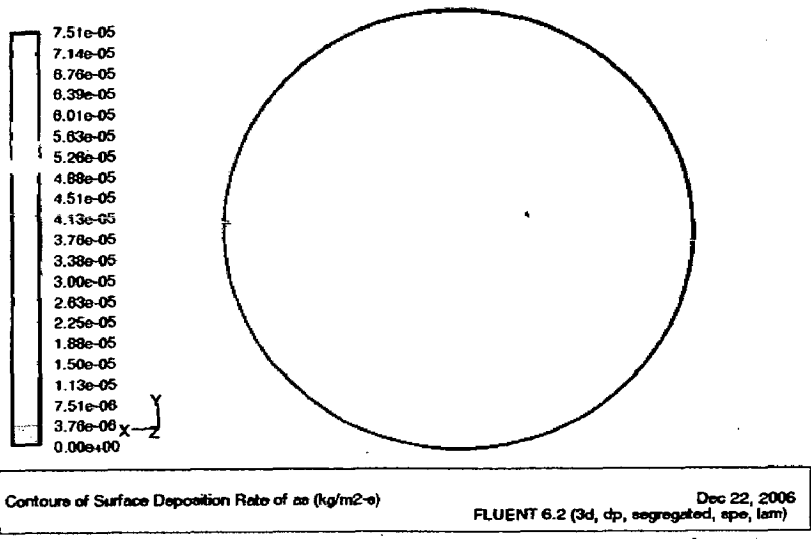


Figure 5.32. Contours of arsenic deposition rate 10rad/s

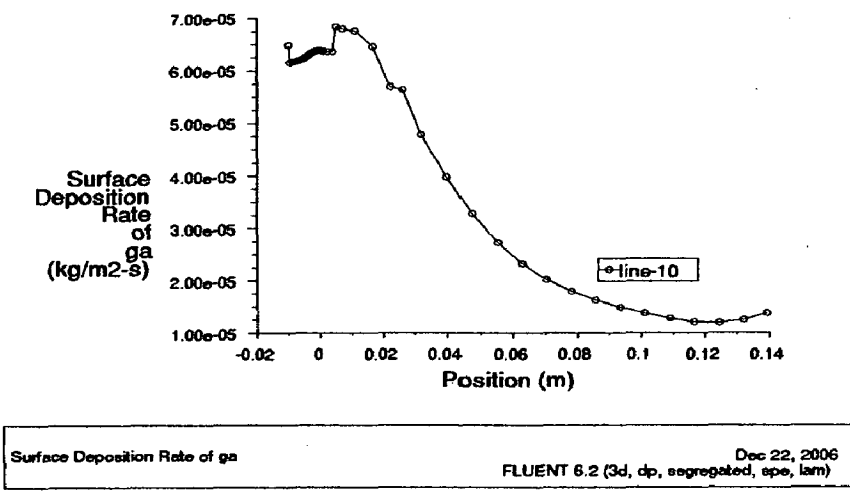


Figure 5.33. Plot of gallium deposition form center to right of the wafer 10rad/s

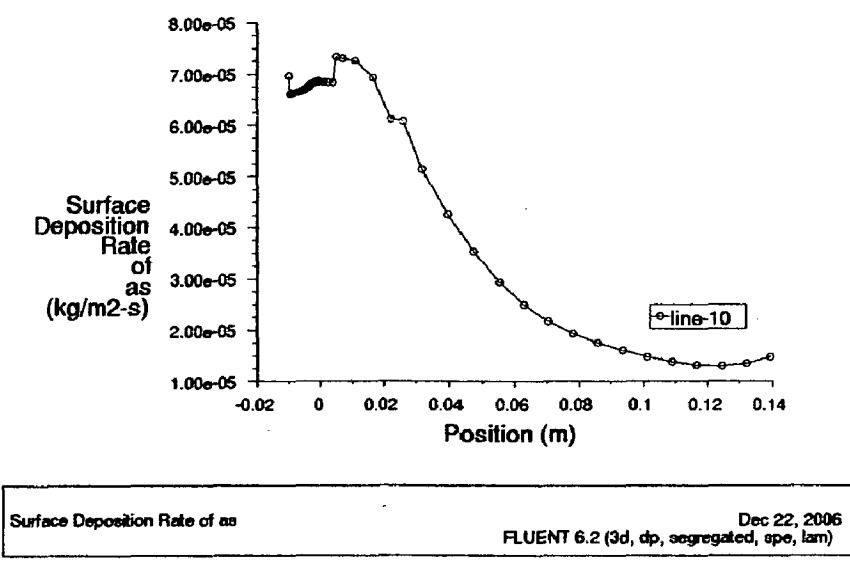


Figure 5.34. Plot of arsenic deposition form center to right of the wafer at 10rad/s

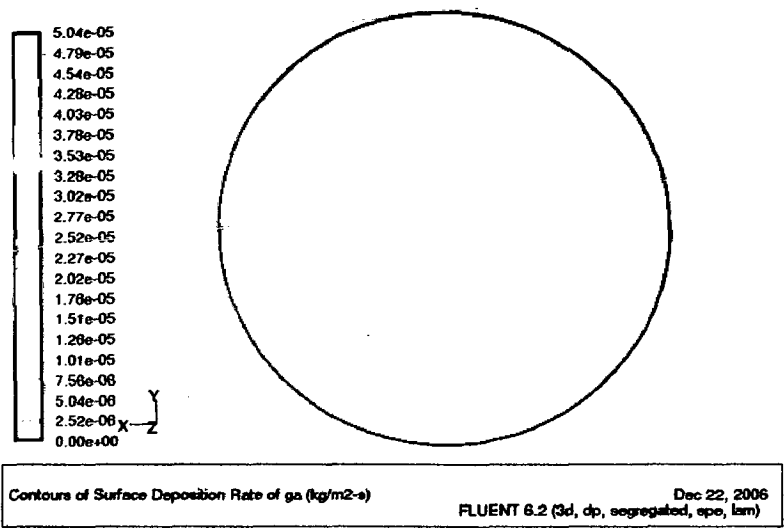


Figure 5.35. Contours of gallium deposition rate at 20rad/s

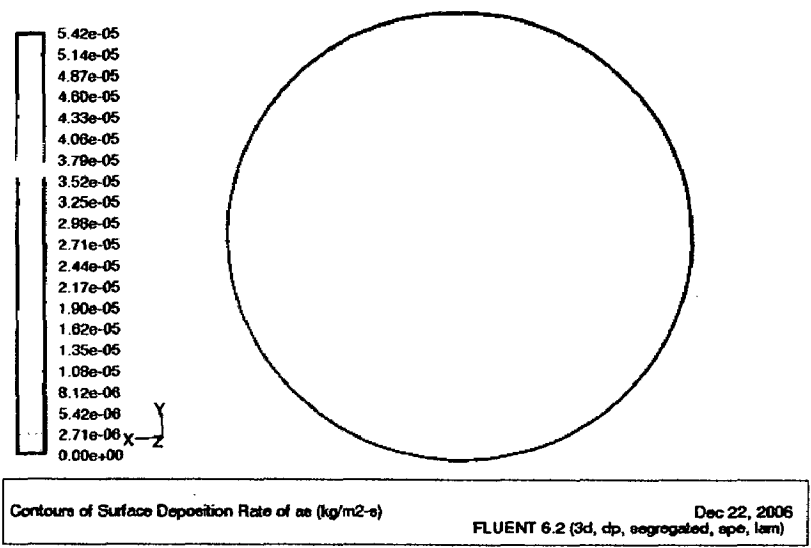


Figure 5.36. Contours of arsenic deposition rate at 20rad/s

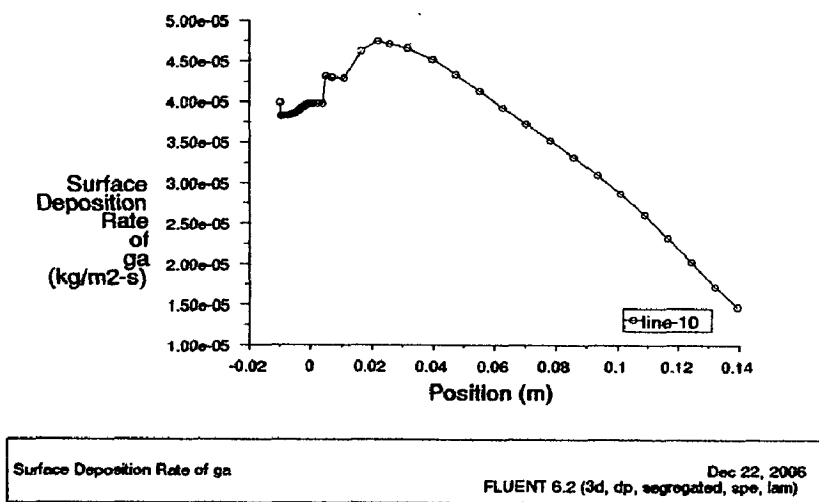
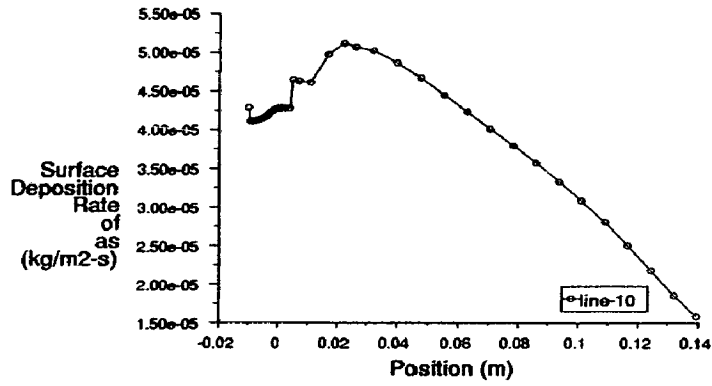
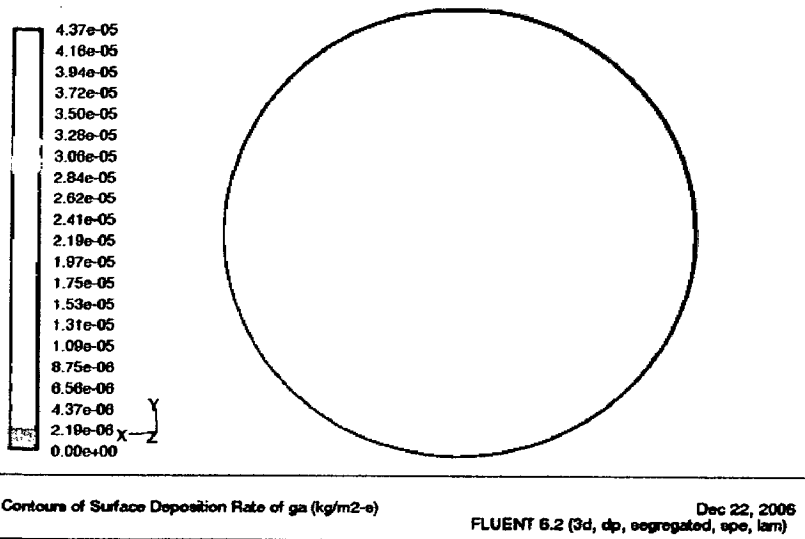


Figure 5.37. Plot of gallium deposition form center to right of the wafer at 20rad/s



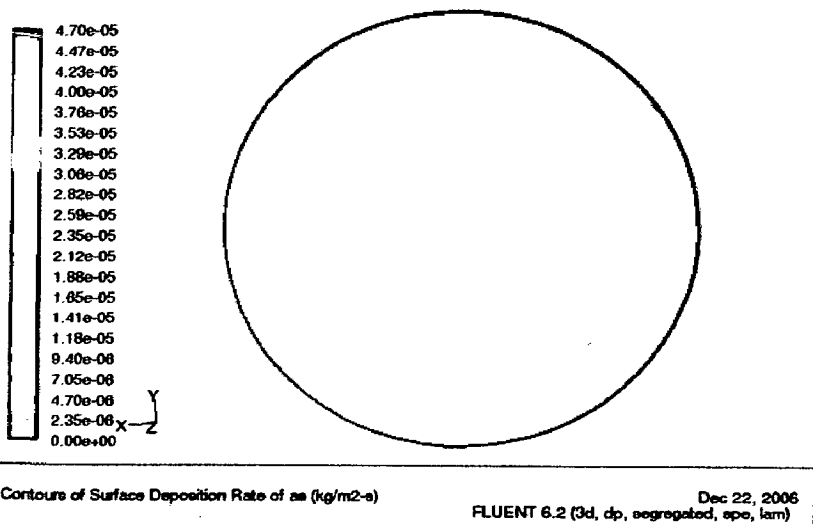
Surface Deposition Rate of As
 FLUENT 6.2 (3d, dp, segregated, spe, lam)
 Dec 22, 2006

Figure 5.38. Plot of arsenic deposition form center to right of the wafer at 20rad/s



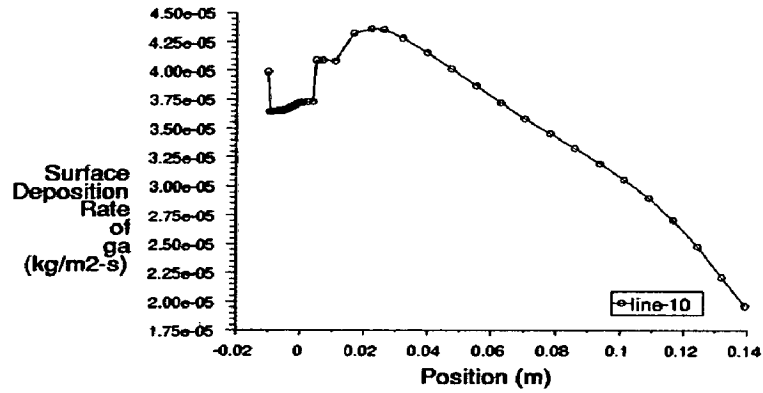
Contours of Surface Deposition Rate of Ga (kg/m²-s)
 FLUENT 6.2 (3d, dp, segregated, spe, lam)
 Dec 22, 2006

Figure 5.39. Contours of Gallium deposition rate at 40rad/s



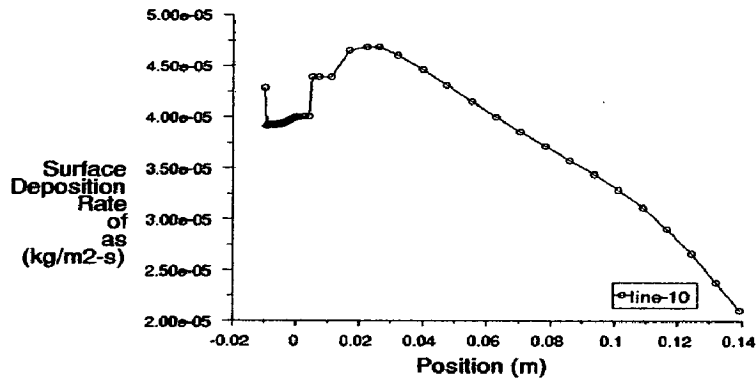
Contours of Surface Deposition Rate of As (kg/m²-s)
 FLUENT 6.2 (3d, dp, segregated, spe, lam)
 Dec 22, 2006

Figure 5.40. Contours of arsenic deposition rate at 40 rad/s



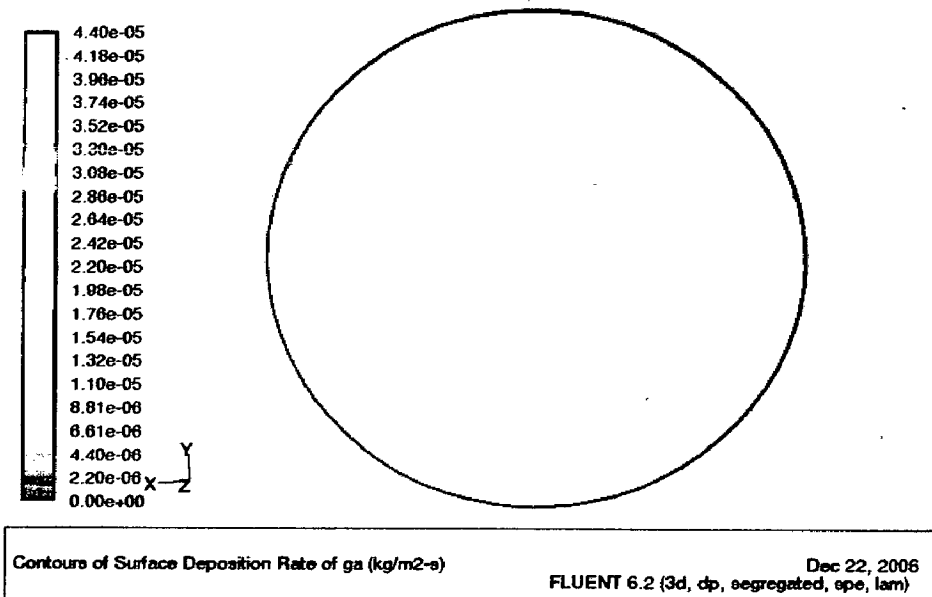
Surface Deposition Rate of ga
 FLUENT 6.2 (3d, dp, segregated, spe, lam) Dec 22, 2006

Figure 5.41. Plot of gallium deposition from center to right of the wafer at 40rad/s



Surface Deposition Rate of as
 FLUENT 6.2 (3d, dp, segregated, spe, lam) Dec 22, 2006

Figure 5.42. Plot of arsenic deposition from center to right of the wafer at 40rad/s



Contours of Surface Deposition Rate of ga (kg/m²-s)
 FLUENT 6.2 (3d, dp, segregated, spe, lam) Dec 22, 2006

Figure 5.43. Contours of gallium deposition rate at 70rad/s

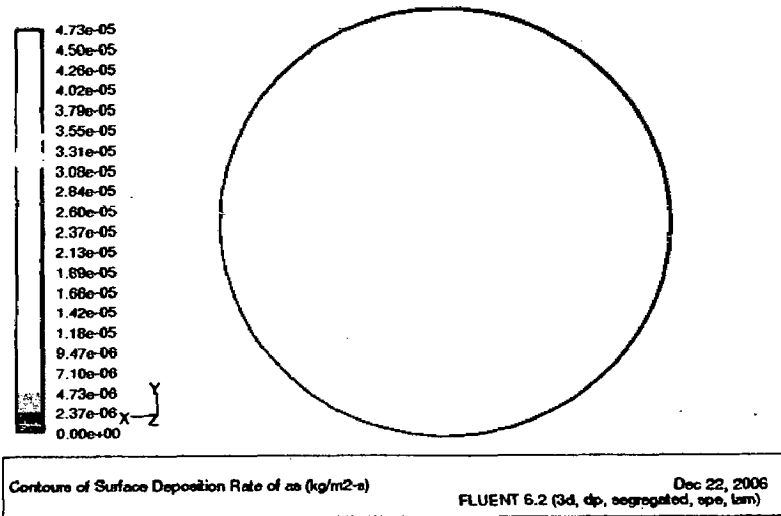


Figure 5.44. Contours of arsenic deposition rate at 70rad/sec

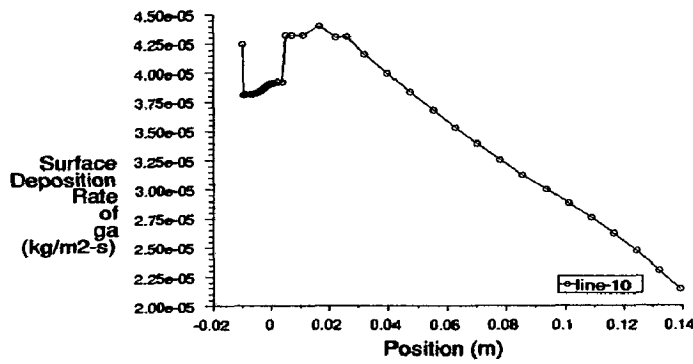


Figure 5.45. Plot of gallium deposition from center to right of the wafer at 70rad/s

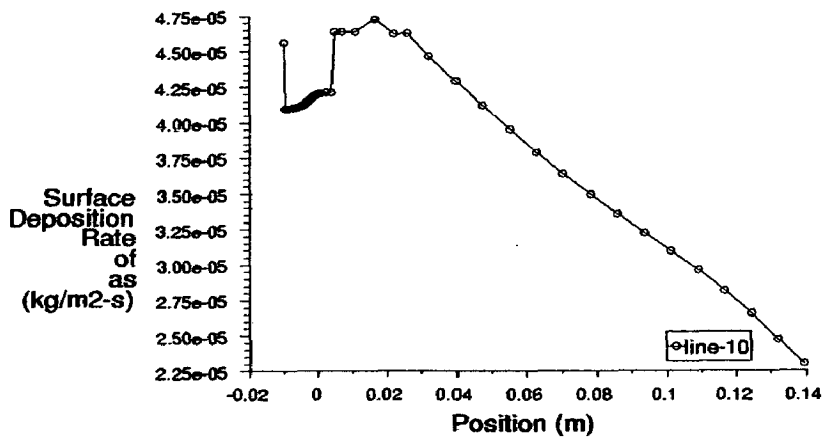


Figure 5.46. Plot of arsenic deposition from center to right of the wafer at 70rad/s

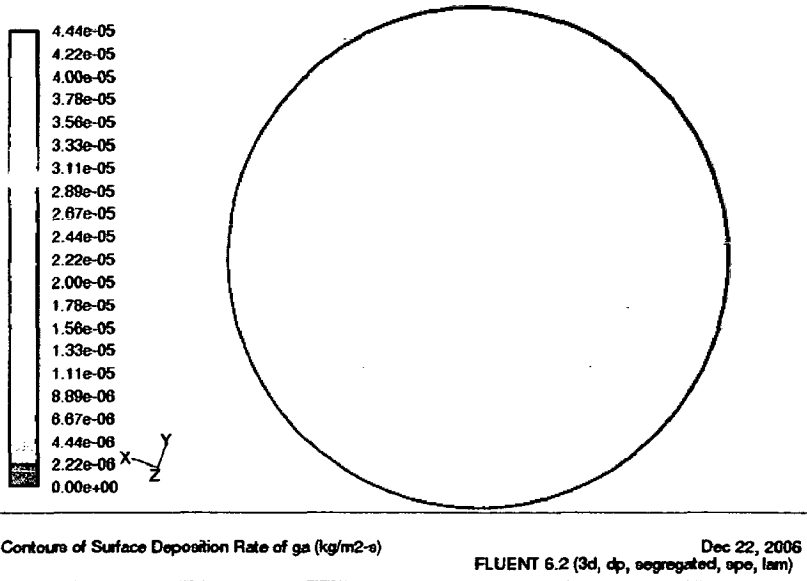


Figure 5.47. Contours of gallium deposition rate at 110rad/s

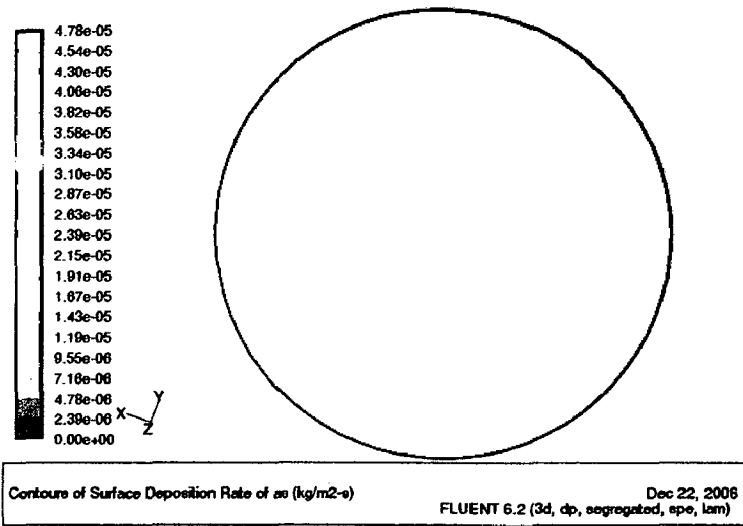


Figure 5.48. Contours of arsenic deposition rate at 110rad/s

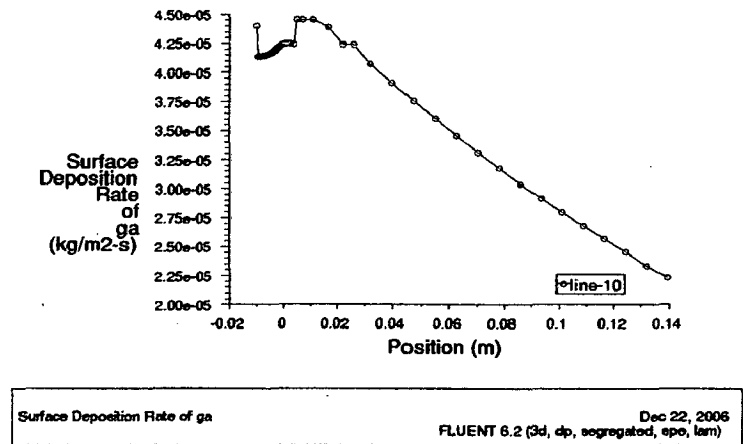
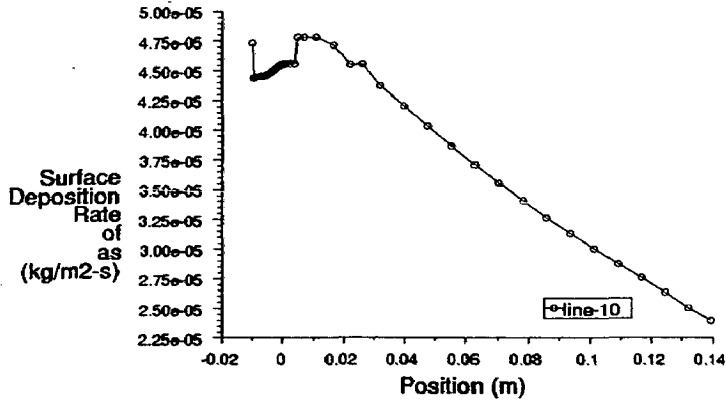
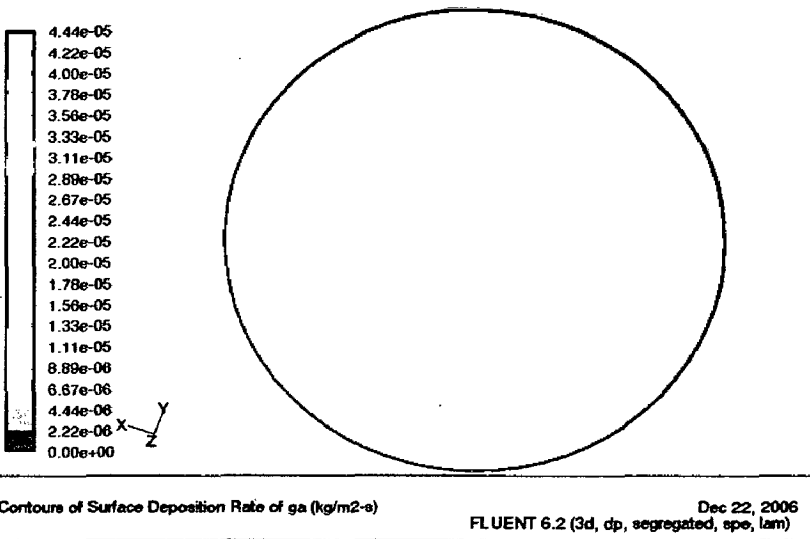


Figure 5.49. Plot of gallium deposition from center to right of the wafer at 110rad/s



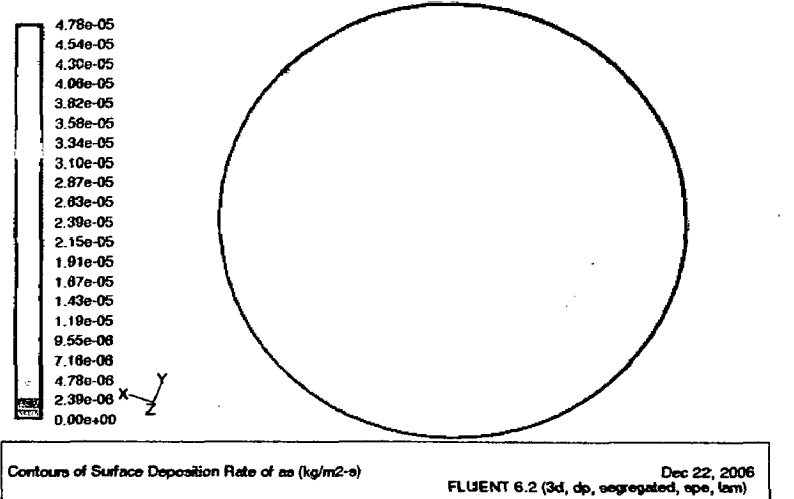
Surface Deposition Rate of as
 FLUENT 6.2 (3d, dp, segregated, spe, lam) Dec 22, 2006

Figure 5.50. Plot of arsenic deposition from center to right of the wafer at 110rad/s



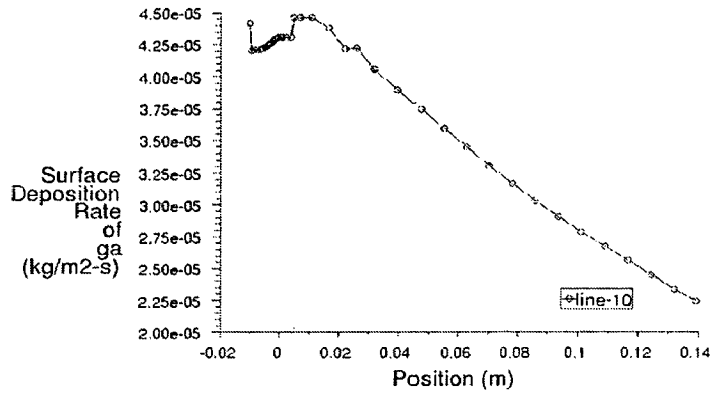
Contours of Surface Deposition Rate of ga (kg/m²-s)
 FLUENT 6.2 (3d, dp, segregated, spe, lam) Dec 22, 2006

Figure 5.51. Contours of gallium deposition rate at 120rad/s



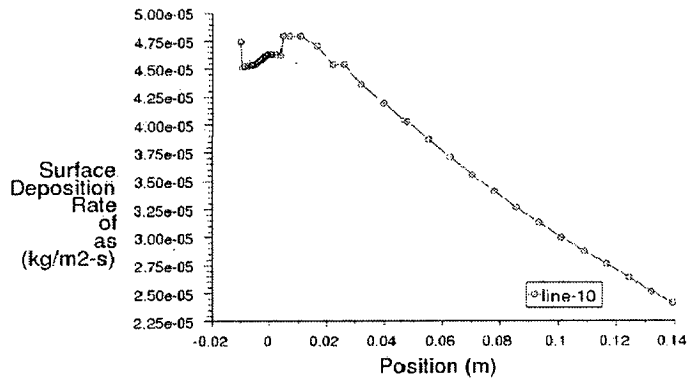
Contours of Surface Deposition Rate of as (kg/m²-s)
 FLUENT 6.2 (3d, dp, segregated, spe, lam) Dec 22, 2006

Figure 5.52. Contours of arsenic deposition rate at 120rad/s



Surface Deposition Rate of ga
 Dec 22, 2006
 FLUENT 6.2 (3d, dp, segregated, spe, lam)

Figure 5.53. Plot of gallium deposition from center to right of the wafer at 120rad/s



Surface Deposition Rate of as
 Dec 22, 2006
 FLUENT 6.2 (3d, dp, segregated, spe, lam)

Figure 5.54. Plot of arsenic deposition from center to right of the wafer at 120rad/s

CONCLUSIONS AND FUTURE SCOPE OF WORK

6. Conclusions and Future scope of work

6.1 Conclusions

In the first problem, 3D turbine vane cooling analysis has been done. Cooling effect has been studied at various time intervals as, 10second 20.37second and 40.74second. The cooling has been achieved at 20.37second. The temperature graph at 40.74second gives out the same result as of 20.37second. It has been found that, the cooled fluid should be injected into the vane with high turbulence; so that vane should get cooled in least time.

For achieving the high turbulence, we have to redesign the vane and plenum system, for avoiding the back pressure smooth corner of small pipe connected with the plenum and vane should be incorporated.

In the second problem, stall has been predicted for axial flow compressor. At various angles of attack, as 10° , 12.5° , 15° and 16° , the contours at 16° shows that the vortices formed at the top of the airfoil covered the largest area. This is responsible for the decrement of the lift and consequently the increment of the drag force. Finally, stall has been registered and the axial flow compressor would not be able to operate.

The optimum angle of attack, 12.5° has been found in this analysis and the practical result of the NASA Langley Research Center also suggested the same. This is the accepted limit. The error analysis shows how best the Spalart-Allamras model fitted into this problem. The several turbulence models have been incorporated in this problem. But, none of them have been converged. This problem has been solved for the compressible flow, and it has been suggested that Spalart-Allamras model is best model for the compressible flow.

In the third problem, CFD has been used for the analysis of the CVD reactor in 3D mode.

The complete physics of the CVD reactor has been employed with efficient manner. The optimization of the wafer rotational speed has been done. This analysis can contribute significantly in the CVD reactor flow design. It has found near about the uniform distribution of the gallium and arsenic at 120rad/s. It has been suggested that optimized speed of the wafer should be 120rad/s. Where velocity 0.02189m/s and wafer temperature 1023K have been kept constant and radius should be 0.14m.

6.2 Future Scope of the work

The analysis contained in the first problem can contribute significantly in the design of the turbine vane.

LES model has been solved for the small scale. It has approved the milestone in the research of the applicability of LES model. Therefore, other small scale problems like film cooling of bearings can be solved with LES model in future.

The simulation contained in the second problem can contribute prominently in the design of the axial flow compressors.

The Spalart-Allamras model has been incorporated and other problems which describe the compressible flow like aerodynamics, missile nozzle flow can be solved with this model in future.

The simulation contained in the third problem can contribute in best way in the design of flow parameter of the CVD reactor.

The problem has been included all the complexity and modeled efficiently can give the way of the solving the other surface chemistry phenomena.

References

1. A-Daini, A. J., Raily, J. W., 'An Actuator-Disc Model for the Prediction of Abrupt Stall in an Axial Compressor Rotor,' International Journal of Heat & Fluid Flow, 1(3), 99-106, September 1979.
2. Asmann, M., Borges, C. F. M., Heberlein, J., Pfender, E., 'The effects of substrate rotation on thermal plasma chemical vapor deposition of diamond', Surface and Coatings Technology, 142-144,724-732, 2001.
3. Azzi, A. A., Jubran, B. A., 'Numerical modeling of film cooling from converging slot-hole', Heat Mass Transfer, 43, 381-388, 2007.
4. Azzi, A., Jubran, B.A., 'Numerical Modeling of Film Cooling from Short Length Stream-Wise Injection Holes', Heat and Mass Transfer 39, 345-353, 2003.
5. Baldwin, B. S., Barth, T. J., 'A One-equation turbulence transport model for high Reynolds number wall-bounded flows', NASA TM 102847, 1990.
6. Baldwin, B. S., Lomax, H., 'Thin layer approximation and algebraic model for separated turbulent flow', AIAA Paper 78-257, 1978.
7. Barakos, G. N., Drikakis, D., 'Computational study of unsteady turbulent flows around oscillating and ramping aerofoils', International journal for numerical methods in fluids, 42, 163-186, 2003.
8. Barakos, G. N., Drikakis, D., 'Unsteady separated flows over manoeuvring lifting surfaces', Philosophical Transactions of the Royal society London A, 358, 3279-3291, 2000.
9. Barathieu, P., Cassaut, B., Schied, E., Couderc, J.P., 'Low-pressure chemical vapor deposition of semi-insulating polycrystalline silicon thin films. II. Theoretical local analysis of the process', Journal of Electrochemical Society, 148(3), C156, 2001.
10. Bliss, D.F., Lynch, C., Weyburne, D., K. O'Hearn, K., Bailey, J. S., 'Epitaxial growth of thick GaAs on orientation-patterned wafers for nonlinear optical applications', Journal of Crystal Growth, 287, 673-678, 2006.
11. Bouteville, A., 'Numerical simulation applied to chemical vapor deposition Process. Rapid thermal CVD and spray CVD', Journal of Optoelectronics and Advanced Materials, 7(2), 599 - 606, April 2005.
12. Breuer, M., 'Large eddy simulation of the subcritical flow past a circular cylinder: numerical and modeling aspects' International Journal of Numerical Methods in Fluids, 28, 1281-1302, 1998.

13. Bui, T.T., '*A parallel, finite-volume algorithm for large-eddy simulation of turbulent flows*', Computers & Fluids, 29, 877–915, 2000.
14. Carter, A.D.S., Andrews, S.J., and Shaw, H., '*Some Fluid Dynamic Research Technique*', Proceedings of Institute of Mechanical Engineering (London), 163, 249-263, 1950.
15. Chae, Y.K., Egashira, Y., Shimogaki, Y., Sugawara, K., Komiyama, H., '*Chemical vapor deposition reactor design using small-scale diagnostic experiments combined with computational fluid dynamics simulations*', Journal of Electrochemical Society 146(5), 1780, 1999.
16. Cho, W.K., Choi, D.H., '*Optimization of a horizontal MOCVD reactor for uniform epitaxial layer growth*', International Journal of Heat Mass Transfer, 43, 1851, 2000.
17. Dearborn, C.H., Saule, H. A., '*Full-scale wind-tunnel and flight test FAIRCHILD 22 air-plane equipped with fowler flap*', Langley Memorial Aeronautical Laboratory, Technical Note No: 578, August 1936.
18. Deardorff, J.W., '*A numerical study of three-dimensional turbulent channel flow at large Reynolds numbers*', Journal of Fluid Mechanics, 41, 453–480, 1970.
19. Donald, C. U., Ronald, J. S., Walter, S. C., '*Stalled and stall-free performance of axial-flow compressor Stage with three inlet-guide-vane and stator-blade settings*', NASA TN D-8457, May 1977.
20. Ericsson, L. E., Reding, J. P., '*Fluid mechanics of dynamic stall Part I: Unsteady flow concepts*', Journal of Fluids and Structures, 2, 1-33, 1988.
21. Ern, A., Vincent Giovangigli, V., Smooke, M. D., '*Detailed modeling of three-dimensional chemical vapor deposition*', Journal of Crystal Growth, 180, 670-679, 1997.
22. Ern, A., Vincent Giovangigli, V., Smooke, M. D., '*Numerical Study of a Three-Dimensional Chemical Vapor Deposition Reactor with Detailed Chemistry*', Journal of computational physics, 126, 21–39, 1996.
23. Fares, E., Schroder, W., '*General One-Equation Turbulence Model for Free Shear and Wall-Bounded Flows*', Flow, Turbulence and Combustion, 73, 187–215, 2004.
24. Firooz, A., Gadami, M., '*Turbulence Flow for NACA 4412 in Unbounded Flow and Ground Effect with Different Turbulence Models and Two Ground Conditions: Fixed and Moving Ground Conditions*', Int. Conference on Boundary and Interior Layers, BAIL 2006.

25. Gauntner, J. W., '*Effects of film injection angle on turbine vane cooling*', NASA TP- 1095, December 1977.
26. Germano, M., Piomelli, U., Moin, P. and Cabot, W.H., '*A dynamic subgrid-scale eddy viscosity mode*', Physics of Fluids A, 7, 1760–1765, 1991.
27. Gottlieb, D., Orszag, S. A., '*Numerical Analysis of Spectral Methods: Theory and Applications*', SIAM, Philadelphia, 1977.
28. Gostelow, J. P., Melwani, N., Walker, G. J., '*Effects of a stream-wise pressure gradient on turbulent spot development. ASME Journal of turbomachinery*', 118, 737-747, 1996.
29. Grujicic, M., Cao, G., Gersten, B., '*Optimization of the chemical vapor deposition process for carbon nanotubes fabrication*', Applied Surface Science, 191, 223, 2002.
30. Heidmann, J. D., Rigby, D. L., Ameri, A. A., '*A Three-Dimensional Coupled Internal/External Simulation of a Film-Cooled Turbine Vane*', Trans. of the ASME, 122, 348-359, April 2000.
31. Hwang, J. Y., Park, C., Huang, M., Anderson, T., '*Investigation of mass transport phenomena in an up flow cold-wall CVD reactor by gas phase Raman spectroscopy and modeling*', Journal of Crystal Growth, 279, 521–530, 2005.
32. Isaev, S. A., Baranov, P. A., Kudryavtsev, N. A., Lysenko, D. A., Usachev, A. E., '*Comparative analysis of the calculation data On an unsteady flow around a circular cylinder Obtained using the VP2/3 and FLUENT packages and the Spalart–Allamaras and Menter Turbulence models*', Journal of Engineering Physics and Thermophysics, 78(6) , 1199-1213, November 2005.
33. Itle, G.C., Salinger, A.G., Pawlowski, R.P., Shadid, J.N., Biegler, L.T., '*A tailored optimization strategy for PDE-based design: application to a CVD reactor*', Computers and Chemical Engineering 28(3), 291, 2004.
34. Kapadia, S., Roy, S., Heidmann, J. D., '*Detached Eddy Simulation of Turbine Blade Cooling*', 36th Thermophysics Conference Orlando, Florida, AIAA, 2003, 3632-3641, 23-26 June 2003.
35. Khanafer, K., Lightstone, M. F., '*Computational modeling of transport phenomena in chemical vapor deposition*', Heat Mass Transfer, 41, 483–494, 2005.
36. Kim, Y-J., Boo, J-H., Hong, B., Kim, Y. J., '*Effects of showerhead shapes on the flow fields in a RF-PECVD reactor*', Surface & Coatings Technology, 193, 88–93, 2005.

37. Kommu, S.K., Wilson, G.M., Khomammi B., '*A theoretical/experimental study of silicon epitaxy in horizontal single-wafer chemical vapor deposition reactors*', Journal of Electrochemical Society, 147(5), 1538, 2000.
38. Lesieur, M., '*Turbulence in Fluids, Third Revised and Enlarged Version*', Kluwer Academic Publishers, Dordrech, 1997.
39. Koshka, Y., Melnychuk, G., Mazzola, M.S., '*Two- and Three-Dimensional Simulation of Chemical Vapor Deposition SiC Epitaxial Growth Processes*', Journal of ELECTRONIC MATERIALS, 32(5), 2003.
40. Liu, N., Ng, E. Y.-K., H. N. Lim, H. N., Tan, T. L., '*Stall prediction of in-flight compressor due to flaming of refueling leakage near inlet*', Computational Mechanics, 30, 479–486, 2003.
41. Maalawi, K. Y., Badr, M. A., '*A practical approach for selecting optimum wind rotors*', Renewable Energy, 28, 803–822, 2003.
42. Majander, P., '*Deveploptions in large eddy simulation*', Helsinki University of Technology, Rep.128, 2000.
43. Marble, Frank E., '*Propagation of Stall in a Compressor Blade Row*', U.S. Air Forces and Guggenheim Jet Propulsion Center, C.I.T., Technical Report 4, Contract AF-18(600)-178, January 1954.
44. Mccroskey, W. J., Mcalister, K. W., Carr, L. W., Pucci, S., '*An experimental study of dynamic stall on advanced airfoil sections*', NASA Technical Memorandum 84245, Volumes 1, 2 and 3, USAAVRADCOM TR-82-A-8, 1982.
45. Patankar, S. V., '*Numerical heat transfer and fluid flow*', Taylor and Francis: Hemisphere, Washington D.C., 1980.
46. Peterson, S.D., Plesniak, M. W., '*Short-hole jet-in-cross flow velocity field and its relationship to film-cooling performance*', Experiments in Fluids, 33, 889–898, 2002.
47. Piomelli, U., Liu, J., '*Large-eddy simulation of rotating channel flows using a localized dynamic mode*', Physics of Fluids, 7(4), 839–848. April 1995.
48. Roy, S., Kapadia, S., Heidmann, J. D., '*Film cooling analysis using DES turbulence model*', Proceedings of ASME Turbo Expo 2003 Power for Land, Sea, and Air, Atlanta, Georgia, USA GT-2003-38140, June 16–19, 2003.
49. Roy, S., Tamamidis, P., '*Numerical investigation of the blade cooling effect Generated by multiple incompressible jets*', Proceedings of FEDSM'98, FEDSM98-4868, Washington, DC, 1998.

50. Sargison, J. E., Oldfield, M. L. G., Guo, S.M., Lock, G. D., Rawlinson, A. J., 'Flow visualization of the external flow from a converging slot-hole film-cooling geometry', *Experiments in Fluids*, 38, 304–318, 2005.
51. Sears, W.R., 'A Theory of "Rotating Stall" in Axial Flow Compressors', Office Sci. Res., U.S. Air Force and Graduate School Aerospace Engineering, Cornell University, Contract AF-33(038) 21406, January 1953.
52. Smagorinsky, J., 'General circulation experiments with the primitive equations, part I: The basic experiment', *Monthly Weather Review*, 91, 99–152, 1963.
53. Smith, A.G., Fletcher, P. J., 'Observations on the Surging of Various Low-Speed Fans and Compressors', Memo. No. M.219, British NGTE, July 1954.
54. Smith, G. D., 'Numerical Solution of Partial Differential Equations: Finite Difference Methods', 3rd edn, Clarendon Press, Oxford, 1985.
55. Spalart, P. R., Allamaras, S. R., 'A one-equation turbulence model for aerodynamic flows', AIAA Paper 92-0439, 30th AIAA Aerospace Sciences Conference, January 1992.
56. Stenning, Alan H., Kriebel, Anthony, R., Montgomery, Stephen, R., 'Stall Propagation in Axial-Flow Compressors', NACA TN 3580, 1956.
57. Tyagi, M., Acharya, S., 'Large Eddy Simulation of Film Cooling Flow from an Inclined Cylindrical Jet', *Trans. of the ASME*, 125, 734-742, October 2003
58. Weber, S., Platzer, M. F., 'Computational simulation of dynamic stall on the NLR 7301 airfoil', *Journal of Fluids and Structures*, 14 (6), 779-798, 2000.
59. Wilson, K., Chiu, S., Jaluria, Y., Glumac, N. G., 'Control of Thin Film Growth in Chemical Vapor Deposition Manufacturing Systems: A Feasibility Study', *Journal of Manufacturing Science and Engineering*, 124, 715-724, August 2002.
60. Xenidou, T.C., Boudouvis, A.G., Tsamakis, D.M., Markatos, N.C., 'An experimentally assisted computational analysis of tin oxide deposition in a cold-wall APCVD reactor', *Journal of Electrochemical Society* 151(12), C757, 2004.
61. Zienkiewicz, O. C., Taylor, R. L., *The Finite Element Method - Vol. 2: Solid and Fluid Mechanics*, McGraw-Hill, New York, 1991.

List of publications

1. **M. Subhash** and C.B. Majumder, 'Film cooling analysis using LES turbulence model', **International Journal of Computational Fluid Dynamics**, Likely to publish in July, 2007.
2. **M. Subhash** and C.B. Majumder, 'Prediction of stall condition for axial-flow compressor using Spalart-Allmaras model', **International Journal of Computational Fluid Dynamics**, Submitted Revised Form.
3. **Maharshi Subhash** and Chandrajit B. Majumder, 'Optimization of operating parameters of Chemical Vapor Deposition Reactor using CFD', **Computers & Chemical Engineering**, Submitted Revised Form.

4.3.3 Solution	40
4.4 Third problem	41-45
4.4.1 The Laminar Finite-Rate Model	42-43
4.4.2 Boundary conditions and material properties	43-45
Chapter 5 RESULTS AND DISCUSSION	46-68
5.1 First Problem	46-51
5.2 Second Problem	51-58
5.3 Third Problem	59-68
Chapter 6 CONCLUSIONS AND FUTURE SCOPE OF THE WORK	69-70
6.1 Conclusions	69
6.2 Future scope of the work	70
REFERENCES	71-75
List of publications	76

LIST OF FIGURES

Fig. No.	Title	Page No.
Figure 1.1	Schematic of the Problem, Front view	9
Figure 3.1	Schematic of the Problem, Front view	26
Figure 3.2	Schematic of the Problem, Top View	27
Figure 3.3	Grid generation field	28
Figure 3.4	Angle of attack (AOA) and chord-length	28
Figure 3.5	Schematic diagram of CVD reactor	29
Figure 5.1	Grid generations by FLUENT6.2	46
Figure 5.2	Static pressure contour at 10sec	46
Figure 5.3	Static pressure contour at 20.37sec	46
Figure 5.4	Static pressure contours at 40.74sec	47
Figure 5.5	Static temperature contours at 10sec	47
Figure 5.6	Static temperature contours at 20.37sec	47
Figure 5.7	Static temperature contours at 40.74sec	48
Figure 5.8	Velocity Vectors at 10sec	48
Figure 5.9	Velocity Vectors at 20.37sec	48
Figure 5.10	Velocity Vectors at 40.74sec	49
Figure 5.11	Static temperature profile at Iso-surface $y=12.74\text{mm}$ (0.5in) after 20.37sec	49

Fig. No.	Title	Page No.
Figure 5.12	Static temperature profile at Iso-surface $y=12.74\text{mm}$ (0.5in) after 40.74sec	49
Figure 5.13	Grid generation around airfoil	52
Figure 5.14	Lift-coefficient at 10° AOA	53
Figure 5.15	Lift-coefficient at 12.5° AOA	53
Figure 5.16	Lift-coefficient at 15° AOA	53
Figure 5.17	Lift-coefficient at 16° AOA	54
Figure 5.18	Drag-coefficient at 10° AOA	54
Figure 5.19	Drag-coefficient at 12.5° AOA	54
Figure 5.20	Drag-coefficient at 15° AOA	55
Figure 5.21	Drag- coefficient at 16° AOA	55
Figure 5.22	Velocity Vectors at 10° AOA	55
Figure 5.23	Velocity Vectors at 12.5° AOA	56
Figure 5.24	Velocity Vectors at 15° AOA	56
Figure 5.25	Velocity Vectors at 16° AOA	56
Figure 5.26	pressure contours at 10° AOA	57
Figure 5.27	pressure contours at 12.5° AOA	57
Figure 5.28	pressure contours at 15° AOA	57
Figure 5.29	Dynamic pressure contours at 16° AOA	58
Figure 5.30	Stall Angle for NACA-2415 airfoil	58
Figure 5.31	Contours of gallium deposition rate 10rad/s	60

4.3.3 Solution	40
4.4 Third problem	41-45
4.4.1 The Laminar Finite-Rate Model	42-43
4.4.2 Boundary conditions and material properties	43-45
Chapter 5 RESULTS AND DISCUSSION	46-68
5.1 First Problem	46-51
5.2 Second Problem	51-58
5.3 Third Problem	59-68
Chapter 6 CONCLUSIONS AND FUTURE SCOPE OF THE WORK	69-70
6.1 Conclusions	69
6.2 Future scope of the work	70
REFERENCES	71-75
List of publications	76

LIST OF TABLES

Table No.	Title	Page No.
Table 4.1	Far-field boundary condition	40
Table 4.2	Solution initialization from Far-Field	40
Table 4.3	AsH3 material properties	44
Table 4.4	Material properties for other chemicals	45
Table 4.5	URF for various parameters	45

LIST OF FIGURES

Fig. No.	Title	Page No.
Figure 1.1	Schematic of the Problem, Front view	9
Figure 3.1	Schematic of the Problem, Front view	26
Figure 3.2	Schematic of the Problem, Top View	27
Figure 3.3	Grid generation field	28
Figure 3.4	Angle of attack (AOA) and chord-length	28
Figure 3.5	Schematic diagram of CVD reactor	29
Figure 5.1	Grid generations by FLUENT6.2	46
Figure 5.2	Static pressure contour at 10sec	46
Figure 5.3	Static pressure contour at 20.37sec	46
Figure 5.4	Static pressure contours at 40.74sec	47
Figure 5.5	Static temperature contours at 10sec	47
Figure 5.6	Static temperature contours at 20.37sec	47
Figure 5.7	Static temperature contours at 40.74sec	48
Figure 5.8	Velocity Vectors at 10sec	48
Figure 5.9	Velocity Vectors at 20.37sec	48
Figure 5.10	Velocity Vectors at 40.74sec	49
Figure 5.11	Static temperature profile at Iso-surface $y=12.74\text{mm}$ (0.5in) after 20.37sec	49

Fig. No.	Title	Page No.
Figure 5.12	Static temperature profile at Iso-surface $y=12.74\text{mm}$ (0.5in) after 40.74sec	49
Figure 5.13	Grid generation around airfoil	52
Figure 5.14	Lift-coefficient at 10° AOA	53
Figure 5.15	Lift-coefficient at 12.5° AOA	53
Figure 5.16	Lift-coefficient at 15° AOA	53
Figure 5.17	Lift-coefficient at 16° AOA	54
Figure 5.18	Drag-coefficient at 10° AOA	54
Figure 5.19	Drag-coefficient at 12.5° AOA	54
Figure 5.20	Drag-coefficient at 15° AOA	55
Figure 5.21	Drag- coefficient at 16° AOA	55
Figure 5.22	Velocity Vectors at 10° AOA	55
Figure 5.23	Velocity Vectors at 12.5° AOA	56
Figure 5.24	Velocity Vectors at 15° AOA	56
Figure 5.25	Velocity Vectors at 16° AOA	56
Figure 5.26	pressure contours at 10° AOA	57
Figure 5.27	pressure contours at 12.5° AOA	57
Figure 5.28	pressure contours at 15° AOA	57
Figure 5.29	Dynamic pressure contours at 16° AOA	58
Figure 5.30	Stall Angle for NACA-2415 airfoil	58
Figure 5.31	Contours of gallium deposition rate 10rad/s	60

Fig. No.	Title	Page No.
Figure 5.32	Contours of arsenic deposition rate 10rad/s	61
Figure 5.33	Plot of gallium deposition form center to right of the wafer 10rad/s	61
Figure 5.34	Plot of arsenic deposition form center to right of the wafer at 10rad/s	61
Figure 5.35	Contours of gallium deposition rate at 20rad/s	62
Figure 5.36	Contours of arsenic deposition rate at 20rad/s	62
Figure 5.37	Plot of gallium deposition form center to right of the wafer at 20rad/s	62
Figure 5.38	Plot of arsenic deposition form center to right of the wafer at 20rad/s	63
Figure 5.39	Contours of Gallium deposition rate at 40rad/s	63
Figure 5.40	Contours of arsenic deposition rate at 40 rad/s	63
Figure 5.41	Plot of gallium deposition from center to right of the wafer at 40rad/s	64
Figure 5.42	Plot of arsenic deposition from center to right of the wafer at 40rad/s	64
Figure 5.43	Contours of gallium deposition rate at 70rad/s	64
Figure 5.44	Contours of arsenic deposition rate at 70rad/sec	65
Figure 5.45	Plot of gallium deposition from center to right of the wafer at 70rad/s	65
Figure 5.46	Plot of arsenic deposition from center to right of the wafer at 70rad/s	65
Figure 5.47	Contours of gallium deposition rate at 110rad/s	66